JGR Oceans

RESEARCH ARTICLE

10.1029/2023JC020833

Key Points:

- We assess whether the mesoscale eddy energy flux divergence can be calculated from sea surface height in the Agulhas Current region
- Geostrophy allows a qualitative estimate of eddy energy advection, but not of eddy pressure work
- This favors the use of sea surface height, but challenges the founding approximations of an earlier paradigm

Correspondence to:

P. Tedesco and J. Gula,
pfmt2@cam.ac.uk;
jonathan.gula@univ-brest.fr

Citation:

Tedesco, P., Gula, J., Penven, P., Ménesguen, C., Jamet, Q., & Vic, C. (2024). Can mesoscale eddy kinetic energy sources and sinks be inferred from sea surface height in the Agulhas Current region? *Journal of Geophysical Research: Oceans*, *129*, e2023JC020833. https://doi.org/10.1029/2023JC020833

Received 21 DEC 2023
Accepted 26 FEB 2024

Author Contributions:

Conceptualization: P. Tedesco
Formal analysis: P. Tedesco
Funding acquisition: J. Gula, C. Ménesguen
Investigation: P. Tedesco
Methodology: P. Tedesco
Supervision: J. Gula, P. Penven, C. Ménesguen
Writing – original draft: P. Tedesco
Writing – review & editing: J. Gula, P. Penven, C. Ménesguen, Q. Jamet, C. Vic

Can Mesoscale Eddy Kinetic Energy Sources and Sinks Be Inferred From Sea Surface Height in the Agulhas Current Region?

P. Tedesco[1,2], J. Gula[1,3], P. Penven[1], C. Ménesguen[1], Q. Jamet[4], and C. Vic[1]

[1]Laboratoire d'Océanographie Physique et Spatiale (LOPS), IUEM, CNRS, IRD, Ifremer, University of Brest, Brest, France, [2]University of Cambridge, Cambridge, UK, [3]Institut Universitaire de France (IUF), Paris, France, [4]INRIA, ODYSSEY Group, Ifremer, Plouzané, France

Abstract Western boundaries have been suggested as mesoscale eddy graveyards, using a diagnostic of the eddy kinetic energy (*EKE*) flux divergence based on sea surface height (η). The graveyard's paradigm relies on the approximation of geostrophy—required by the use of η—and other approximations that support long baroclinic Rossby waves as the dominant contribution to the *EKE* flux divergence. However, a recent study showed an opposite paradigm in the Agulhas Current region using an unapproximated *EKE* flux divergence. Here, we assess the validity of the approximations used to derive the η-based *EKE* flux divergence using a regional numerical simulation of the Agulhas Current. The *EKE* flux divergence consists of the eddy pressure work (*EPW*) and the *EKE* advection (*AEKE*). We show that geostrophy is valid for inferring *AEKE*, but that all approximations are invalid for inferring *EPW*. A scale analysis shows that at mesoscale ($L > O(30)$ km), *EPW* is dominated by coupled geostrophic-ageostrophic *EKE* flux and that Rossby waves effect is weak. There is also a hitherto neglected topographic contribution, which can be locally dominant. *AEKE* is dominated by the geostrophic *EKE* flux, which makes a substantial contribution (54%) to the net regional mesoscale *EKE* source represented by the *EKE* flux divergence. Other contributions, including topographic and ageostrophic effects, are also significant. Our results support the use of η to infer a qualitative estimate of the *EKE* flux divergence in the Agulhas Current region. However, they invalidate the approximations on mesoscale eddy dynamics that underlie the graveyard's paradigm.

Plain Language Summary In the ocean, the most energetic motions are large-scale eddies with horizontal scales ranging from tens to hundreds of kilometers. These are major components of the ocean energy budget, and unraveling their lifecycles is crucial to improving our understanding of ocean dynamics. Although the generation of large-scale eddies is well documented, how their energy is dissipated remains uncertain. Based on satellite observations of the sea surface and approximations to the dynamics of large-scale eddies, it has been suggested that they decay at western boundaries of oceanic basins, thereby closing their lifecycle. However, based on different data and approximations, a recent study has suggested that large-scale eddies are predominantly generated in a specific western boundary region, such as the Agulhas Current. Our study explains which of the data (sea surface observations) or the assumed leading order dynamics (approximations) explains the opposite eddy energy sources and sinks shown by the two studies in the Agulhas Current region. Our results show that the use of sea surface observations is valid for qualitatively inferring the regional eddy energy source, but not the assumed leading order dynamics. This has implications for (a) our understanding and (b) study strategies of the energetics of large-scale eddies.

1. Introduction

Mesoscale eddies account for 80% of the surface kinetic energy and are a key component of the global ocean energy budget (Ferrari & Wunsch, 2009; Müller et al., 2005; Wunsch, 2007). They have horizontal scales of the order of the first Rossby deformation radius (*Rd*) or larger (Chelton et al., 2011). At these scales, the velocity field can be decomposed into a leading order geostrophic and a weaker ageostrophic component, following the quasi-geostrophic theory (Gill, 1982). Geostrophic flows are horizontally divergence-free flows—in a local approximation—dominated by the effects of rotation compared to advection (Rossby number: $Ro \ll 1$) and stratification compared to vertical shear (Richardson number: $Ri \gg 1$). Ageostrophic flows account for variations in the geostrophically balanced system. They are characterized by a large vertical component and the increasing effects of advection.

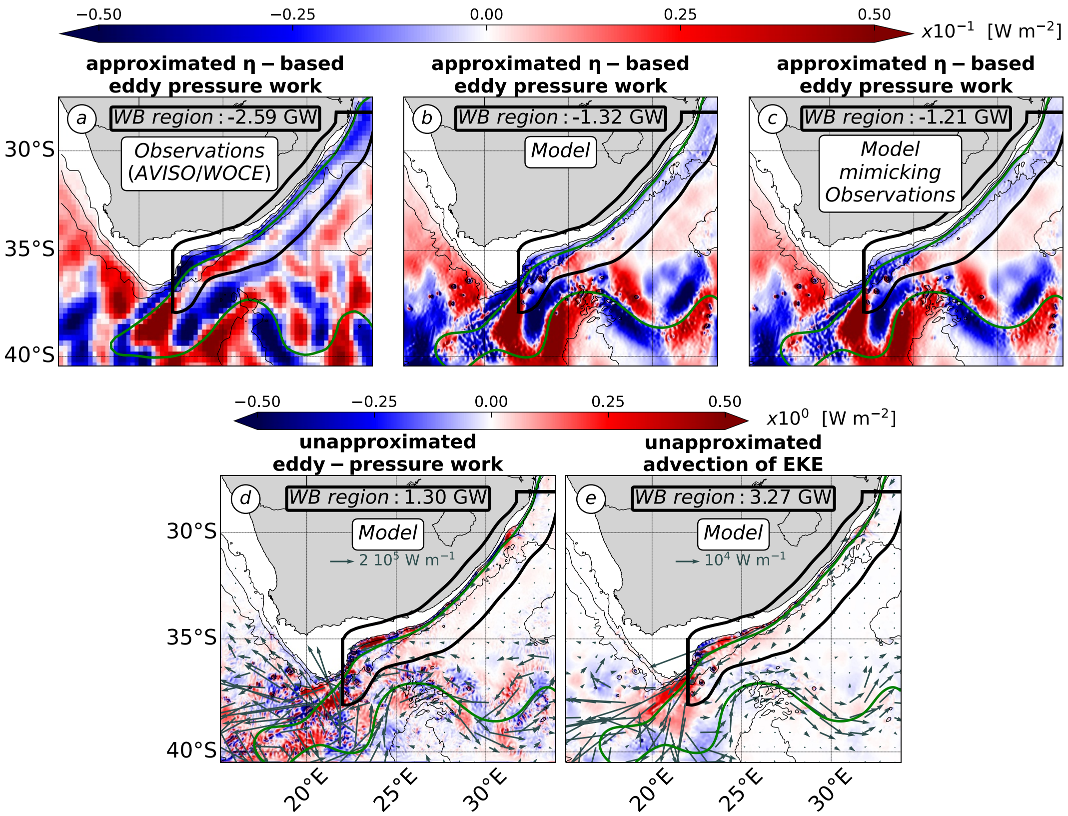

Figure 1. Different versions of the mesoscale *EKE* flux divergence (formed by eddy pressure work and advection of *EKE*) [W m^{-2}] in the Agulhas Current region. (a-c) Approximated η-based EPW performed from (a) observations (AVISO and WOCE data) following Zhai et al. (2010) and (b and c) a numerical simulation (built upon the CROCO model), at (b) the resolution of the simulation (dx ~2.5 km) and (c) a coarsened resolution mimicking the resolution of observations. (d and e) Unapproximated model-based (d) EPW and (e) advection of *EKE* at the resolution of the simulation (dx ~2.5 km). Note the different colorbar ranges between panels (a–c) and panels (d and e). Black area denotes the western boundary (WB) region. The cumulative terms in the WB region are in [GW] (10^{9} W). Green contours denote the 0.25 m isoline of time-averaged η and black contours denote 1,000 m and 3,000 m isobaths.

Mesoscale eddies are easily tracked by satellite altimetry, which measures sea surface height (η) and whose low-frequency component is an indirect measure of surface geostrophic currents. Satellite altimetry has shown that mesoscale eddies are ubiquitous in the oceans and that they are most energetic in western boundary (WB) currents and in the Antarctic Circumpolar Current (Chelton et al., 2007, 2011; Ducet et al., 2000). This identifies these regions as key to the global ocean energy budget.

Using satellite altimetry data, Zhai et al. (2010) suggested western boundaries as mesoscale eddy kinetic energy (*EKE*) sinks. In the energy budget, sources and sinks of *EKE* are accounted for by the *EKE* flux divergence term (Harrison & Robinson, 1978). This term represents the rate of *EKE* transport done by: the work of pressure fluctuations the eddy pressure work (EPW; usually interpreted as the linear contribution from waves) and the nonlinear advection of *EKE* by mean and eddy flows. When ocean dynamics are in equilibrium, the *EKE* flux divergence indicates a net *EKE* source (>0) or sink (<0).

Zhai et al. (2010) explicitly developed a η-based diagnostic of the mesoscale EPW (linear component of the *EKE* flux divergence) using several approximations. Their diagnosis reduces to the linear contribution of the β-effect, corresponding in particular to the propagation of long Rossby waves. Figure 1a shows Zhai et al. (2010)'s version of the EPW in the Agulhas Current region, which they suggested to be the largest mesoscale *EKE* sink. The approximated η-based EPW indicates an almost uniform mesoscale *EKE* sink (<0) at the western boundary (WB; black domain), whose cumulative value is of $O(1)$ GW (Figure 1a).

Their result would establish the following paradigm: mesoscale eddies originate almost everywhere in the ocean, propagate westward at about the speed of long baroclinic Rossby waves, and decay at western boundaries, probably through direct energy routes to dissipation, channeled by topography (Chelton et al., 2011; Evans et al., 2022; Gill et al., 1974; Zhai et al., 2010). This scenario is supported in regions free of WB currents, by in situ measurements and idealized numerical simulations (Evans et al., 2020, 2022; Z. Yang et al., 2021). However, in regions containing WB currents, model-based studies suggest more complex mesoscale eddy dynamics. Western boundaries are hotspots for mesoscale eddy generation due to instabilities of the WB currents (Gula et al., 2015; Halo et al., 2014; Kang & Curchitser, 2015; Jamet et al., 2021; Li et al., 2021; Tedesco et al., 2022; Yan et al., 2019; Y. Yang & Liang, 2016).

In particular, a recent study has shown that the Agulhas Current region is a mesoscale *EKE* source using an unapproximated *EKE* flux divergence performed from a model (Tedesco et al., 2022). Figures 1d and 1e shows the unapproximated EPW and advection of *EKE* (forming the *EKE* flux divergence) computed from three-dimensional modeled mesoscale velocities (Tedesco et al., 2022). Both unapproximated terms differ significantly from the approximated η-based EPW, with their magnitudes being larger of an order and their scale patterns smaller (Figures 1d and 1e). In the WB region of the Agulhas Current, the two unapproximated terms are the most intense on the shelf—over a band narrower than the WB width—and have locally comparable magnitudes. Their cumulative value represents a mesoscale *EKE* source (>0), whose main contribution is due to the advection of *EKE*.

The opposite mesoscale *EKE* sources and sinks supported in the Agulhas Current region by the different versions of the *EKE* flux divergence (Figures 1a, 1d, and 1e reproducing Tedesco et al., 2022; Zhai et al., 2010), challenge (a) the hypothesis that long baroclinic Rossby waves are the main contributors to the mesoscale *EKE* flux divergence, and thus (b) the approximations used to derive the η-based term. In this study, we focus on explaining the differences between the approximated η-based and the unapproximated model-based *EKE* flux divergence in the Agulhas Current region. We discuss below the approximations used by Zhai et al. (2010) and their implications:

1. **Mesoscale *EKE* flux divergence is mainly due to geostrophic flows**: The geostrophic approximation is required when using satellite altimetry data. Geostrophy is a good approximation to infer mesoscale eddy velocities, which have small Rossby numbers ($Ro = O(\ll 0.05)$; Chelton et al., 2011). However, the use of geostrophic velocities to infer the mesoscale *EKE* flux divergence—a tendency term of the *EKE* budget that represents the rate of spatial redistribution of the mesoscale *EKE* reservoir (Harrison & Robinson, 1978)—is a separate issue.
2. **The vertical structure of mesoscale eddies is represented by the first baroclinic mode**: The sea surface height (η) is usually interpreted as primarily reflecting surface-intensified vertical structures represented by the first baroclinic mode. However, the mesoscale *EKE* reservoir is represented by the combination of the barotropic and first baroclinic modes (Smith & Vallis, 2001; Venaille et al., 2011; Wunsch, 1997). The partitioning between the two vertical modes varies regionally, from being close to equipartition to being dominated by one of the modes (Tedesco et al., 2022; Yankovsky et al., 2022). The contributions of the barotropic and first baroclinic modes to the mesoscale *EKE* flux divergence remain unknown to our knowledge. Their individual contributions can possibly transport *EKE* in a decoupled (coupled) manner, which would then compensate (accumulate) when considering the *EKE* flux divergence for the mesoscale reservoir.
3. **Mesoscale *EKE* flux interactions with topography are weak**: The approximation of weak topographic interactions is equivalent to assuming that the mesoscale *EKE* flux has spatial variations larger than those of topography (Zhai et al., 2010). This approximation is challenged by (a) the large topographic gradients at western boundaries ($1 \times 10^{-2} \pm 2 \times 10^{-2}$ in the Agulhas Current region) and (b) the strong topographic control on mesoscale eddy dynamics at western boundaries. Topography controls the triggering of current' instabilities that generate mesoscale eddies (Gula et al., 2015; Lutjeharms, 2006) and helps to channel energy transfers between mesoscale eddies and other types of flow (Adcock & Marshall, 2000; Evans et al., 2020; Nikurashin & Ferrari, 2010; Perfect et al., 2020; Tedesco et al., 2022). The contribution of topography to the mesoscale *EKE* flux divergence remains, to our knowledge, an open question.

In summary, opposing paradigms of mesoscale eddy dynamics are supported by two versions of the diagnosis of the *EKE* flux divergence in the WB region of the Agulhas Current (Tedesco et al., 2022; Zhai et al., 2010). The two diagnoses differ in method (η field measured by satellite altimetry vs. modeled 3-dimensional velocities) and assumed leading order contribution to the *EKE* flux divergence (long baroclinic Rossby waves as a result of approximations (i), (ii) and (iii) vs. no approximations to account for geostrophic, ageostrophic and topographic contributions acting on the barotropic and first baroclinic mode). The two contradictory diagnoses of mesoscale *EKE* source and sink suggest that either the method or the approximations lead to a misestimation of the mesoscale *EKE* flux divergence. This raises questions about the main contributions to the dynamics of the mesoscale eddy energy reservoir, and consequently, about strategies for studying mesoscale eddies. Open questions include: What are the main contributions—among geostrophic and ageostrophic effects, barotropic and first baroclinic modes, and topographic contribution—to the EPW and advection of *EKE*? What are the implications for inferring the mesoscale *EKE* flux divergence using the η field? We focus in particular on determining whether approximation (i) of geostrophy is valid, as it is the only one formally required for the use of satellite altimetry to infer the mesoscale *EKE* flux divergence.

In the present study, we use a numerical simulation to evaluate the validity of approximation (i) for inferring the mesoscale *EKE* flux divergence in the region of the Agulhas Current. Our study is organized as follows. Unapproximated and η-based expressions of the EPW and advection of *EKE* (which form the *EKE* flux divergence) are presented in Section 2. The regional numerical simulation is presented in Section 3. The unapproximated and η-based versions of the EPW and advection of *EKE* are evaluated in Sections 4, 5 and 6. Finally, we discuss our results in the larger context of altimetry-based diagnosis of mesoscale eddy dynamics at western boundaries in Section 7.

2. Theory

In this section we present the modal *EKE* flux divergence. First, we present the theoretical framework of the vertical modes. Then, we define the unapproximated expression of the modal *EKE* flux divergence, which consists of the EPW and the advection of *EKE* (*AEKE*). Finally, we define the η-based expressions of *EPW* and *AEKE*.

2.1. Vertical Modes

A convenient approach to describe the vertical structure of mesoscale motions is the modal decomposition using traditional vertical modes (Gill, 1982). The vertical structure of the mesoscale *EKE* reservoir corresponds to the combination of the barotropic and first baroclinic modes (Smith & Vallis, 2001; Tedesco et al., 2022; Venaille et al., 2011; Wunsch, 1997), which represents surface-intensified vertical structures energized to the bottom.

The vertical modes ϕ_n for the horizontal velocity ($\mathbf{u}$) and the dynamical pressure (p) are the eigenfunctions solution of the Sturm-Liouville problem (Equation 1), using linearized free-surface $\left(| \frac{\partial}{\partial z}\phi_n|_{z=\eta} = |\frac{-\overline{N^2}}{g}\phi_n|_{z=\eta} \right)$ and flat-bottom boundary conditions $\left(| \frac{\partial}{\partial z}\phi_n|_{z=-H} = 0 \right)$:

$$\frac{\partial}{\partial z}\left(\frac{1}{N^2}\frac{\partial}{\partial z}\phi_n\right) + \frac{1}{c_n^2}\phi_n = 0 \tag{1}$$

with N^2 the time-averaged buoyancy frequency, g the acceleration of gravity and $c_n^2 = \frac{1}{n\pi}\int_{-H}^{\eta} N(\mathbf{x}, z)\, dz$ the eigenvalues of the vertical modes.

The modal base ϕ_n satisfies the orthogonality condition:

$$\int_{-H}^{\eta} \phi_m \phi_n \, dz = \delta_{mn} h \tag{2}$$

with δ_{mn} the usual Kronecker symbol and $h = \eta + H$ the water column depth.

The dynamical variables are projected onto n vertical modes as follows:

$$\left[\mathbf{u}_n(\mathbf{x}, t), \frac{1}{\rho_0} p_n(\mathbf{x}, t)\right] = \frac{1}{h}\int_{-H}^{\eta}\left[\mathbf{u}(\mathbf{x}, z, t), \frac{1}{\rho_0} p(\mathbf{x}, z, t)\right]\phi_n(\mathbf{x}, z)\, dz \tag{3}$$

with $\mathbf{u}_n$ and p_n the modal amplitudes of the horizontal velocity ($\mathbf{u}$) and dynamical pressure (p) and ρ_0 the reference density value.

The vertical modes are related to horizontal scales via c_n^2, which are good approximations of the Rossby baroclinic deformation radii: $Rd_{n \geq 1} = \frac{c_n}{|f|}$ (Chelton et al., 1998), with f the Coriolis parameter.

2.2. Unapproximated Modal *EKE* Flux Divergence

2.2.1. *EKE* Flux Divergence in the *EKE* Budget

The modal *EKE* flux divergence is a term of the modal *EKE* budget. A comprehensive modal *EKE* budget has been derived in Tedesco et al. (2022), inspired from the budget derived in the context of internal tides (Kelly, 2016). The modal *EKE* budget reads as follows:

$$\begin{aligned} &\underbrace{\mathbf{u}_n' \cdot \left(\rho_0 h \frac{\partial}{\partial_t} \mathbf{u}_n'\right)}_{Time\ rate} \quad + \underbrace{\underbrace{\nabla_H \cdot \int_{-H}^{\eta} \mathbf{u}_n' p_n' \phi_n^2 \, dz}_{Eddy-pressure\ work\ (EPW)} + \underbrace{\frac{\rho_0}{2} \nabla_H \cdot \int_{-H}^{\eta} \mathbf{u}_n \phi_n \|\mathbf{u}_n' \phi_n\|^2 \, dz}_{Advection\ of\ EKE\ (AEKE)}}_{EKE\ flux\ divergence\ (EPW+AEKE)} \\ &= \sum \left(\underbrace{S_n}_{EKE\ sources} + \underbrace{D_n}_{EKE\ sinks} \right) \end{aligned} \tag{4}$$

Terms are time-averaged and the primes indicate fluctuations relative to the time-average. The dynamical pressure ($p(\mathbf{x}, z, t)$) is derived from the in situ density ($\rho(\mathbf{x}, z, t)$) from which the background density profile ($\tilde{\rho}(z)$, defined as the spatial and temporal average of the in situ density) has been subtracted.

The *EKE* flux divergence corresponds to the rate of *EKE* spatial transport. When integrated over a domain, the *EKE* flux divergence corresponds to the transport across the domain boundaries. A positive (negative) sign indicates that outgoing (incoming) flux dominate the incoming (outgoing) flux. At equilibrium, the time rate of *EKE* (Equation 4) is negligible. The *EKE* flux divergence is therefore equal to the sum of the *EKE* sources and sinks accounted for in the right-hand side of the modal *EKE* budget (S_n and D_n in Equation 4). A positive (negative) *EKE* flux divergence thus represents a net *EKE* source (sink) that is then transported away (has been transported in).

The *EKE* flux divergence consists of two contributions: the eddy pressure work (*EPW*; Equation 4) and the advection of *EKE* by the mean and eddy flows (*AEKE*; Equation 4) (Harrison & Robinson, 1978). *EPW* is the only contribution to the *EKE* flux divergence in the context of linear theories of internal waves (Kelly, 2016; Kelly et al., 2010, 2012) and of Rossby waves (Masuda, 1978). It is also the main contribution for interior-ocean dynamics (Harrison & Robinson, 1978). *AEKE* can contribute significantly to the *EKE* flux divergence and can be equivalent to *EPW* in regions of high variability (Capó et al., 2019; Harrison & Robinson, 1978; Tedesco et al., 2022).

Here, we study the *EKE* flux divergence for the mesoscale reservoir over the period 1995–2004. We define the mesoscale *EKE* flux divergence as the sum of the barotropic ($n = 0$) and first baroclinic ($n = 1$) contributions: $EPW_{n=0-1}$ and $AEKE_{n=0-1}$. To simplify notations, we refer to the mesoscale terms as *EPW* and *AEKE* in the following. The modeled mesoscale eddy dynamics over the period 1995–2004 is in equilibrium. The smallness of the time rate of *EKE* (Equation 4) has been asserted for the period 1995–1999 in Tedesco et al. (2022). It is even smaller for the period 1995–2004 considered in this study.

2.2.2. Contributions to the *EKE* Flux Divergence

EPW and *AEKE* (Equation 4) can be written as the sum of the contributions of *EKE* flux ($A + B$ in Equations 5 and 6) and *EKE* flux interacting with topographic gradients (C in Equations 5 and 6) as follows:

$$EPW = \underbrace{\underbrace{\int_{-H}^{\eta} p_n'\phi_n \nabla_H \cdot \left(\mathbf{u}_n'\phi_n\right)\, dz}_{velocity\ \ divergence\ \ (\mathbf{A})} + \underbrace{\int_{-H}^{\eta} \left(\mathbf{u}_n'\phi_n\right) \cdot \nabla_H\left(p_n'\phi_n\right)\, dz}_{work\ \ of\ \ eddy\ \ pressure\ \ shear\ \ (\mathbf{B})}}_{EKE\ \ flux\ \ (\mathbf{A+B})} \\ + \underbrace{\nabla_H\eta \cdot \left|\mathbf{u}_n'p_n'\phi_n^2\right|_{z=\eta} + \nabla_H H \cdot \left|\mathbf{u}_n'p_n'\phi_n^2\right|_{z=-H}}_{topographic-contribution\ \ (\mathbf{C})} \tag{5}$$

$$AEKE = \underbrace{\underbrace{\frac{\rho_0}{2}\int_{-H}^{\eta} \|\mathbf{u}_n'\phi_n\|^2 \nabla_H \cdot \left(\mathbf{u}_n\phi_n\right)\, dz}_{velocity\ \ divergence\ \ (\mathbf{A})} + \underbrace{\frac{\rho_0}{2}\int_{-H}^{\eta} \left(\mathbf{u}_n\phi_n\right) \cdot \nabla_H\|\mathbf{u}_n'\phi_n\|^2\ dz}_{work\ \ of\ \ EKE\ \ shear\ \ (\mathbf{B})}}_{EKE\ \ flux\ \ (\mathbf{A+B})} \\ \underbrace{+\frac{\rho_0}{2}\nabla_H\eta \cdot \left|\mathbf{u}_n\phi_n\|\mathbf{u}_n'\phi_n\|^2\right|_{z=\eta} + \frac{\rho_0}{2}\nabla_H H \cdot \left|\mathbf{u}_n\phi_n\|\mathbf{u}_n'\phi_n\|^2\right|_{z=-H}}_{topographic-contribution\ \ (\mathbf{C})} \tag{6}$$

The *EKE* flux term ($A + B$; Equations 5 and 6) consists of a velocity divergence contribution (A) and an eddy pressure shear work for *EPW* (B in Equation 5) and an *EKE* shear work for *AEKE* (B in Equation 6). From their analytical expressions, it can be deduced that the importance of geostrophic and ageostrophic effects varies between A and B. The velocity divergence contributions (A) mainly account for ageostrophic effects, since geostrophic velocities are horizontally divergent-free. The only geostrophic effects in A are due to geostrophic velocities expressed in the β-plane (Cushman-Roisin & Beckers, 2011). The geostrophic A-contributions acting on *EPW* and *AEKE* are thus reduced to *EKE* flux driven by the β-effect. In the case of *EPW* (Equation 5), the β-driven linear *EKE* flux corresponds to long baroclinic Rossby waves and was assumed by Zhai et al. (2010) to be the primary contributor to *EPW*, and subsequently to the *EKE* flux divergence. The work contribution (B) accounts for geostrophic and ageostrophic effects in different proportions for *EPW* and *AEKE*. For *EPW* (Equation 5), the B-contribution is exclusively due to ageostrophic effects. Indeed, geostrophic velocities are orthogonal to the eddy pressure shear resulting in the cancellation of the eddy pressure shear work. For *AEKE* (Equation 6), the B-contribution accounts for both geostrophic and ageostrophic effects. Geostrophic velocities are in the same direction than the *EKE* shear, resulting in a non-null work.

The topographic-contribution (C; Equations 5 and 6) acting on *EPW* and *AEKE* represents the interactions of *EKE* flux with topography and sea surface height gradients. It can be reduced to the contribution of topography gradients, which are much larger than η gradients ($\|\nabla_H\eta\| = O(10^{-4})\|\nabla_H H\|$). The analytical expression of C does not allow the contribution of geostrophic or ageostrophic effects to be readily separated.

2.3. Approximated η-Based Modal *EKE* Flux Divergence

In the following, we present the η-based expressions of *EPW* and *AEKE* accounting for approximation (i). We also present two other η-based expressions of *EPW* accounting for approximations (ii) and (iii). The main expressions of *EPW* and *AEKE* discussed in this study are listed in Tables 1 and 2.

2.3.1. Approximations (I) of Geostrophic Velocities ($EPW_{(i)}$ and $AEKE_{(i)}$)

Approximation (i) of geostrophy is required by the use of η to infer the *EKE* flux divergence. *EPW* and *AEKE* are written as $EPW_{(i)}$ and $AEKE_{(i)}$ when using modal geostrophic velocities (Tables 1 and 2). Modal geostrophic velocities are expressed from η fields, modulated to account for the fraction of the different vertical modes with $\lambda_n = \frac{\eta_n}{\eta}$ and $\alpha_n = \frac{\eta_n'}{\eta'}$, as follows:

$$\mathbf{u}_{g,n}\phi_n = \mathbf{k}\wedge\frac{g}{f}\nabla_H\left(\frac{\phi_n}{|\phi_n|_{z=0}}\lambda_n\eta\right) \tag{7}$$

$$\mathbf{u}_{g,n}'\phi_n = \mathbf{k}\wedge\frac{g}{f}\nabla_H\left(\frac{\phi_n}{|\phi_n|_{z=0}}\alpha_n\eta'\right) \tag{8}$$

Table 1
Summary of the Unapproximated and η-Based Versions of the Eddy Pressure Work (EPW)

Acronyms	Analytical expressions	Descriptions
EPW	$\underbrace{\nabla_H \cdot \int_{-H}^{\eta} \mathbf{u}'_n p'_n \phi_n^2 \, dz}_{(A+B+C)}$	Unapproximated mesoscale eddy pressure work
$EPW_{(i)}$	$\underbrace{-\frac{\beta\rho_0 g^2}{2f^2}\frac{\partial}{\partial x}\left(\frac{\int_{-H}^{\eta}\phi_n^2\,dz}{\lvert\phi_n^2\rvert_{z=0}}\alpha_n^2\eta'^2\right)}_{\beta-contribution\ (A1)} + \underbrace{\frac{\beta\rho_0 g^2}{2f^2}\frac{\partial H}{\partial x}\frac{\lvert\phi_n^2\rvert_{z=-H}}{\lvert\phi_n^2\rvert_{z=0}}\alpha_n^2\eta'^2}_{\beta-driven\ topographic-contribution\ (A2)}$ $+\underbrace{\frac{\rho_0 g^2}{2f}\nabla_H H \cdot \mathbf{k}\wedge\nabla_H\left(\frac{\lvert\phi_n^2\rvert_{z=-H}}{\lvert\phi_n^2\rvert_{z=0}}\alpha_n^2\eta'^2\right)}_{topographic-contribution\ (C)}$, with $\alpha_n = \frac{\eta'_n}{\eta'}$	Unapproximated η-based version of mesoscale eddy pressure work (use of approximation (i))
$EPW_{(i,ii)}$	$\underbrace{-\frac{\beta\rho_0 g^2}{2f^2}\frac{\partial}{\partial x}\left(\frac{\int_{-H}^{\eta}\phi_1^2\,dz}{\lvert\phi_1^2\rvert_{z=0}}\eta'^2\right)}_{\beta-contribution\ (A1)} + \underbrace{\frac{\beta\rho_0 g^2}{2f^2}\frac{\partial H}{\partial x}\frac{\lvert\phi_1^2\rvert_{z=-H}}{\lvert\phi_1^2\rvert_{z=0}}\eta'^2}_{\beta-driven\ topographic-contribution\ (A2)}$ $+\underbrace{\frac{\rho_0 g^2}{2f}\nabla_H H \cdot \mathbf{k}\wedge\nabla_H\left(\frac{\lvert\phi_1^2\rvert_{z=-H}}{\lvert\phi_1^2\rvert_{z=0}}\eta'^2\right)}_{topographic-contribution\ (C)}$	Approximated η-based version of mesoscale eddy pressure work (use of approximations (i) and (ii))
$EPW_{(i,ii,iii)}$	$\underbrace{-\frac{\beta\rho_0 g^2}{2f^2}\frac{\partial}{\partial x}\left(\frac{\int_{-H}^{\eta}\phi_1^2\,dz}{\lvert\phi_1^2\rvert_{z=0}}\eta'^2\right)}_{\beta-contribution\ (A1)}$	Approximated η-based version of mesoscale eddy pressure work defined by Zhai et al. (2010) (use of approximations (i), (ii) and (iii))

Table 2
Summary of the Unapproximated and η-Based Versions of the Advection of Mesoscale EKE (AEKE)

Acronyms	Analytical expressions	Descriptions
AEKE	$\underbrace{\frac{\rho_0}{2}\nabla_H \cdot \int_{-H}^{\eta} \mathbf{u}_n \phi_n \lVert \mathbf{u}'_n \phi_n \rVert^2 \, dz}_{(A+B+C)}$	Unapproximated advection of mesoscale *EKE*
AEKE$_{(i)}$	$\underbrace{-\frac{\beta \rho_0 g}{2 f^2} \int_{-H}^{\eta} \lVert \mathbf{u}'_{g,n} \phi_n \rVert^2 \frac{\partial}{\partial x}\left(\frac{\phi_n}{\lvert \phi_n \rvert_{z=0}} \lambda_n \eta\right) dz}_{velocity\ \ divergence\ \ (A)} +$ $\underbrace{\frac{\rho_0}{2} \int_{-H}^{\eta} \left(\mathbf{u}_{g,n} \phi_n\right) \cdot \nabla_H \lVert \mathbf{u}'_{g,n} \phi_n \rVert^2 \, dz}_{work\ \ of\ \ EKE\ \ shear\ \ (B)}$ $+\underbrace{\frac{\rho_0}{2} \nabla_H H \cdot \left\lvert \mathbf{u}_{g,n} \phi_n \lVert \mathbf{u}'_{g,n} \phi_n \rVert^2 \right\rvert_{z=-H}}_{topographic-contribution\ \ (C)}$, with $\lambda_n = \frac{\eta_n}{\eta}$	Unapproximated η-based version of advection of mesoscale *EKE* (use of approximation (i))

Approximation (i) of geostrophy has a larger impact on *EPW* than on *AEKE*. $EPW_{(i)}$ (Table 1) reduces to a linear *EKE* flux driven by the β-effect ($A1$) and two topographic contributions, one acting on the β-driven *EKE* flux ($A2$) and the other acting on geostrophic *EKE* flux (C). $AEKE_{(i)}$ (Table 2) includes the β-effect (A), the geostrophic *EKE* shear work (B) and a topographic contribution acting on the geostrophic *EKE* flux (C).

2.3.2. Approximations (II) and (III) ($EPW_{(i,ii)}$ and $EPW_{(i,ii,iii)}$)

The η-based version of *EPW* defined by Zhai et al. (2010) relies on the additional approximations (ii) and (iii), which are not formally required by the use of η to infer the *EKE* flux divergence. Approximations (ii) and (iii) therefore lead to approximated versions of the η-based *EPW*: $EPW_{(i,ii)}$ and $EPW_{(i,ii,iii)}$ (Table 1).

2.3.2.1. Approximation (II) of Sea Surface Height Primarily Reflecting the First Baroclinic Mode ($EPW_{(i,ii)}$)

$EPW_{(i,ii)}$ is written as $EPW_{(i)}$, but assumes that modal geostrophic velocities expressed from η reflect only the first baroclinic mode (Table 1), using $\alpha_n \sim \alpha_1 \sim 1$, as follows:

$$\mathbf{u}'_{g,1}\phi_1 = \mathbf{k}\wedge\frac{g}{f}\nabla_H\left(\frac{\phi_1}{|\phi_1|_{z=0}}\eta'\right) \tag{9}$$

2.3.2.2. Approximation (III) of Weak Topographic-Contributions ($EPW_{(i,ii,iii)}$)

$EPW_{(i,ii,iii)}$ ($A1$; Equation 10) is derived from $EPW_{(i,ii)}$ ($A1 + A2 + C$), assuming that topographic contributions ($A2$ and C) are negligible:

$$EPW_{(i,ii,iii)} = \underbrace{-\frac{\beta\rho_0 g^2}{2f^2}\frac{\partial}{\partial x}\left(\frac{\int_{-H}^{\eta}\phi_1^2\,dz}{|\phi_1^2|_{z=0}}\eta'^2\right)}_{\beta-contribution\ \ (\mathbf{A1})} \tag{10}$$

$EPW_{(i,ii,iii)}$ ($A1$; Table 1) corresponds to a β-driven linear *EKE* flux acting on the first baroclinic mode, which represents the contribution of long baroclinic Rossby waves to the *EKE* flux divergence. $EPW_{(i,ii,iii)}$ is the approximated η-based version of *EPW* used in Zhai et al. (2010), which established the paradigm of mesoscale eddies decay at western boundaries.

This study focuses on evaluating the main contributions to *EPW* and *AEKE* (which form the *EKE* flux divergence) in the Agulhas Current region (Figures 1d and 1e). To do this, we evaluate the impacts of approximations (i), (ii) and (iii) on *EPW* and of approximation (i) on *AEKE*. We start our analysis by *EPW*, which is the term explicitly discussed in Zhai et al. (2010). We first evaluate the validity of approximations (ii) and (iii) to infer the η-based *EPW* (cf., Section 4). This allows us to define $EPW_{(i)}$—the unapproximated η-based *EPW*—which we then use to evaluate the validity of approximation (i) of geostrophy to infer the unapproximated *EPW* (cf., Section 5). We next expand our analysis to *AEKE* (cf., Section 6). This term dominates the cumulative value of the *EKE* flux divergence in the WB region (Figure 1e) and is not explicitly discussed in Zhai et al. (2010).

Evaluation of the effects of approximations (i), (ii), and (iii) on *EPW* provides information on the elements of mesoscale eddy dynamics that invalidate the paradigm of mesoscale eddy graveyard in the Agulhas Current region. In addition, evaluation of the effect of approximation (i) of geostrophy on *EPW* and *AEKE* provides information on the possibility of using η to infer *EKE* flux divergence.

3. Method

In this section, we present and evaluate the regional numerical simulation of the Agulhas Current. We first present the numerical set-up and observations used in this study. We then evaluate the modeled mesoscale eddy dynamics against observations. The modeled mesoscale *EKE* in the Agulhas Current region has already been evaluated against satellite altimetry data in Tedesco et al. (2022). Here, we evaluate the η-based version of *EKE* flux divergence defined by Zhai et al. (2010) ($EPW_{(i,ii,iii)}$) derived from our numerical simulation against one derived from observations. The computation of $EPW_{(i,ii,iii)}$ ($A1$; Table 1) requires the computation of vertical modes—based on the time-averaged stratification (N^2)—and η.

3.1. Numerical Model

The regional numerical simulation of the Agulhas Current was performed using the Coastal and Regional COmmunity (CROCO) model. It is a free surface model, based on ROMS (Shchepetkin & McWilliams, 2005), which solves the primitive equations in the Boussinesq and hydrostatic approximations using a terrain following coordinate system (Debreu et al., 2012). The numerical simulation is presented in details in Tedesco et al. (2022). The simulation has a horizontal resolution of dx ∼2.5 km and 60 vertical levels. It encompasses the Agulhas Current region from its source (north of the Natal Bight at 27°S) to the Agulhas Retroflection (at ∼37°S), from where it becomes the Agulhas Return Current. Boundary conditions are supplied by two lower-resolution grids (dx ∼22.5 and 7.5 km, respectively covering most of the South Indian Ocean and its western part).

Vertical modes are derived from the time-averaged stratification over the period 1995–2004, computed from the modeled daily-averaged temperature and salinity.

3.2. Observations

The WOCE (World Ocean Circulation Experiment) climatology provides in situ temperature and salinity fields at a global scale for monthly compositing means at the horizontal resolution of 1° (Gouretski & Koltermann, 2004).

Altimetric data are mapped on a regular 1/4°-grid by AVISO (Archiving, Validation and Interpretation of Satellite Oceanographic data) and provide global scale η field for weekly compositing means. We focus on a subset of data over the Agulhas Current region (15°− 34°E and 27°–40°S) for the period 1995–2004.

3.3. Observed and Modeled Mesoscale *EKE* Sources and Sinks From $EPW_{(i,ii,iii)}$

Figures 1a–1c shows $EPW_{(i,ii,iii)}$ (Table 1) in the Agulhas Current region calculated from observations and the model. Observed and modeled $EPW_{(i,ii,iii)}$ show patterns in fairly good agreement in the Agulhas Current region. $EPW_{(i,ii,iii)}$ is most intense at the Retroflection and along the Agulhas Return Current ($O(0.1–0.5)$ W m^{-2}), where it has patterns altering positive and negative signs. It is less intense along the Agulhas Current and in the Subgyre ($O(0.01–0.1)$ W m^{-2}), where it has more uniform patterns.

We define the WB region as extending from north of the Natal Bight (∼27°S) to the African tip (∼37°S), over a typical width for a WB current of about 150 km (black region in Figure 1). In the WB region, $EPW_{(i,ii,iii)}$ is roughly uniformly negative, indicating an *EKE* sink of cumulative magnitude $O(1)$ GW. This is consistent with the *EKE* sink emphasized by Zhai et al. (2010) at the WB of the South Indian Ocean (poleward of 10°S).

Observed and modeled $EPW_{(i,ii,iii)}$s differ mainly in the magnitude of the *EKE* sinks that they depict in the WB region. There is about a twofold decrease in the model compared to the observations (Figures 1a–1c). The difference in magnitude is not explained by the coarser horizontal resolution of AVISO data (effective horizontal resolution of $O(100)$ km; Chelton et al., 2011) compared to the model (effective horizontal resolution of 25 km; following Soufflet et al., 2016). The twofold decrease in the model is also present when using smoothed modeled η, with a length scale of 100 km to mimic the altimetry data processing done by AVISO (Figure 1c). This indicates that the net *EKE* sink in the WB region is robust to altimetry data processing and that horizontal scales $<O(100)$ km do not contribute significantly to $EPW_{(i,ii,iii)}$. The difference in magnitude could be explained by too weak a forcing of remotely generated eddies in the model. The numerical simulation is forced at the boundaries by a parent simulation (dx ∼7.5 km), which resolves mesoscale eddies of scales 50–100 km, but underestimate their amplitude. See Appendix A for details of the evaluation of the amplitude of the modeled mesoscale eddy field against satellite altimetry data. This underestimation in the model is likely due to a too weak inverse cascade at smaller scales, which have been shown to substantially energize the mesoscale eddy energy reservoir in the Agulhas Current region (Schubert et al., 2020). Note that the magnitude of the cumulative *EKE* flux is sensitive to the definition of the WB region. Our definition of the WB region best captures the *EKE* sink shown by the modeled and observed $EPW_{(i,ii,iii)}$. However, the observed *EKE* sink extends further south of the WB region (Figure 1a), while the modeled one is fully encompassed by the WB region—with its southern face closely following the 0 W m^{-2} isoline—(Figures 1c and 1d).

The fairly good agreement between modeled and observed *EKE* reservoirs (Tedesco et al., 2022) and $EPWs_{(i,ii,iii)}$ (Figures 1a–1c), indicates that our numerical simulation reliably represents the mesoscale eddy dynamics, at least as inferred from satellite altimetry data. Our numerical simulation is therefore suitable to evaluate the leading

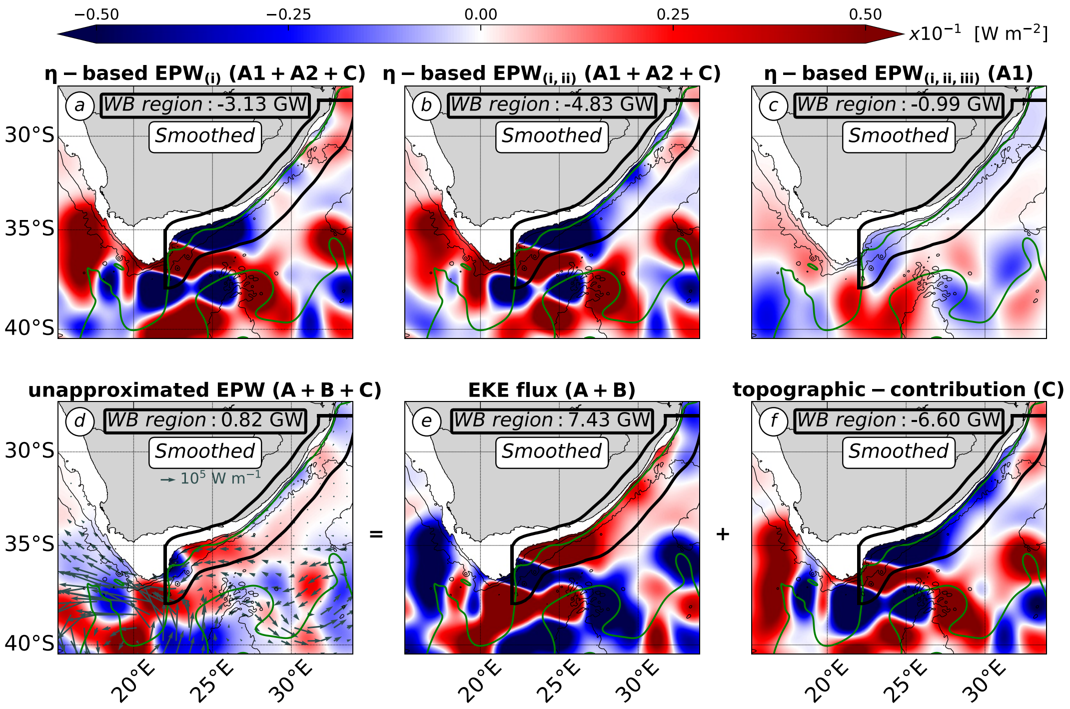

Figure 2. η-based and unapproximated EPWs [W m^{-2}] (Table 1). (a-c) Versions of η-based EPW, including (a) $EPW_{(i)}$, (b) $EPW_{(i,ii)}$, and (c) $EPW_{(i,ii,iii)}$. (d) Unapproximated EPW ($A + B + C$) split into the contributions of (e) EKE flux ($A + B$) and (c) topographic-contribution (C). Terms are smoothed with a 75 km-radius Gaussian kernel. (cf., Figure 1 for a detailed caption).

order contribution of the *EKE* flux divergence, and subsequently to explain the opposing paradigms between η-based and unapproximated diagnoses in this region.

4. Approximated and Unapproximated η-Based *EPWs* ($EPW_{(i,ii,iii)}$ and $EPW_{(i)}$)

In this section, we evaluate the validity of approximations (ii) and (iii) to reliably infer the η-based $EPW_{(i)}$. We first compare $EPW_{(i)}$ (unapproximated η-based EPW) and $EPW_{(i,ii,iii)}$ (approximated η-based EPW used by Zhai et al., 2010). Next, we detail separately the differences due to approximations (ii) and (iii).

Note that most of the figures discussed in the study show smoothed terms (Figures 2 and 4; Figure B1). Smoothed terms highlight the large-scale patterns driving the cumulative contributions in the WB region. Smoothing also facilitates comparison between $EPW_{(i,ii,iii)}$ (Figures 1a–1c) and the other EPW versions. The smoothing length scale corresponds to a typical mesoscale eddy radius at mid-latitudes (75 km), as inferred from satellite altimetry (Chelton et al., 2011). See Appendix B for details on the sensitivity of EPW to the smoothing length scale.

4.1. Mesoscale *EKE* Sources and Sinks From the Unapproximated and Approximated η-Based *EPWs* ($EPW_{(i)}$ vs. $EPW_{(i,ii,iii)}$)

Figures 2a–2c shows the different versions of the η-based EPW in the Agulhas Current region ($EPW_{(i)}$, $EPW_{(i,ii)}$ and $EPW_{(i,ii,iii)}$). $EPW_{(i)}$ and $EPW_{(i,ii,iii)}$ have different local patterns and magnitudes in the Agulhas Current region (Figures 2a and 2c). In the WB region, $EPW_{(i)}$ is predominantly negative, but shows patterns of varying magnitude and sign (Figure 2a). This contrasts with $EPW_{(i,ii,iii)}$ which is almost uniformly negative (Figure 2c). Both EPWs show an EKE sink in the WB region, but that of $EPW_{(i)}$ (−3.13 GW) is significantly larger than that of $EPW_{(i,ii,iii)}$ (−0.99 GW).

The differences between $EPW_{(i)}$ and $EPW_{(i,ii,iii)}$ show that $EPW_{(i,ii,iii)}$—the approximated η-based version of EPW defined by Zhai et al. (2010)—is not a good estimate of the unapproximated η-based $EPW_{(i)}$ in the Agulhas Current region (Figures 2a and 2c). This indicates that one or both of the approximations (ii) and (iii) are not valid for inferring the η-based $EPW_{(i)}$.

4.2. Bias Due To Approximation (II)

Approximation (ii) of η primarily reflecting the first baroclinic mode can bias the η-based $EPW_{(i,ii)}$ in two ways. It can bias the accurate estimate of the contribution of the first baroclinic mode to the η-based $EPW_{(i)}$. η does not exclusively reflect eddies (η variance) of the first baroclinic mode. In the WB region of the Agulhas Current, the variance of the modeled η accounts for about 16% ± 4% of the barotropic mode, 38 ± 4% of the first baroclinic mode and 36% ± 2% of a coupling between the first 10 vertical modes (Figure C1). See Appendix C for details on the partitioning of the η variance into the 10 first vertical modes in the Agulhas Current region. Approximation (ii) may also bias the estimate of the *EKE* flux divergence for the mesoscale reservoir, because $EPW_{(i,ii)}$ does not include the barotropic contribution. Contributions from the barotropic and first baroclinic $EPW_{(i)}s$ can transport *EKE* in a decoupled (coupled) manner, which would then compensate (accumulate) when considering the *EKE* flux divergence for the mesoscale reservoir.

$EPW_{(i,ii)}$ and $EPW_{(i)}$ have similar local patterns and magnitudes in the Agulhas Current region (Figures 2a and 2b). However, their cumulative *EKE* sinks differ slightly in the WB region. $EPW_{(i,ii)}$ denotes a larger *EKE* sink (−4.83 GW; Figure 2b) than $EPW_{(i)}$ (−3.13 GW; Figure 2a). $EPW_{(i,ii)}$ includes only the contribution from the first baroclinic mode, while $EPW_{(i)}$ can be split into the contributions of the barotropic mode (−1.01 GW in the WB region; not shown) and the first baroclinic mode (−2.12 GW in the WB region; not shown).

The large similarities between $EPW_{(i)}$ and $EPW_{(i,ii)}$ patterns (Figures 2a and 2b) indicate that approximation (ii) is not the main reason for the large discrepancies between $EPW_{(i)}$ and $EPW_{(i,ii,iii)}$ in the Agulhas Current region (Figures 2a and 2c). However, approximation (ii) leads to an overestimation of (a) the *EKE* sink in the WB region (overestimation by 154%) and (b) the contribution of the first baroclinic mode (overestimation by 228%).

4.3. Bias Due To Approximation (III)

The topography acts on $EPW_{(i,ii)}$ ($A1 + A2 + C$; Table 1) via two contributions: the β-driven flux ($A2$) and the geostrophic *EKE* flux (C). Approximation (iii) of weak topographic contribution is equivalent to assuming that the mesoscale *EKE* flux ($A1$) has larger spatial variations than that of the topography ($A2$ and C) (Zhai et al., 2010).

$EPW_{(i,ii)}$ and $EPW_{(i,ii,iii)}$ have very different patterns and magnitudes in the Agulhas Current region (Figures 2b and 2c). These differences are the same as those for $EPW_{(i)}$ and $EPW_{(i,ii,iii)}$ (cf., Section 4.1). This confirms that approximation (iii) is the one that limits the estimate of the η-based $EPW_{(i)}$ in the Agulhas Current region (Figures 2a–2c). This also indicates that the topographic contributions ($A2$ and C in $EPW_{(i)}$ and $EPW_{(i,ii)}$; Table 1) dominate the η-based *EPW*s ($EPW_{(i)}$ and $EPW_{(i,ii)}$; Figures 2a and 2b). In particular, the topographic contribution to the geostrophic *EKE* flux (C: −4.54 GW in the WB region; not shown) is the dominant contribution, compared to the β-driven topographic contribution ($A2$: 0.70 GW in the WB region; not shown).

In summary, $EPW_{(i,ii,iii)}$—the *EPW* version defined by Zhai et al. (2010)—is not a good estimate of $EPW_{(i)}$—the unapproximated η-based *EPW*—in the Agulhas Current region, because approximation (iii) is not valid (Figures 2a–2c). In other words, the β-driven linear *EKE* flux acting on the first baroclinic mode ($EPW_{(i,ii,iii)}$) is not the leading order contribution to the η-based $EPW_{(i)}$. $EPW(i)$ ($A1 + A + 2 + C$; Figure 1a) is dominated by interactions between the geostrophic *EKE* flux of the barotropic and first baroclinic modes with topographic gradients (C).

However, the η-based $EPW_{(i)}$ still shows an *EKE* sink in the WB region (<0; Figure 2a) in contrast with the unapproximated *EPW* (>0; Figure 1d). This suggests that approximation (i) of geostrophy is the one at the origin of the opposing paradigms supported by η-based and unapproximated *EPW*.

5. η-Based $EPW_{(i)}$ and Unapproximated *EPW*

In this section, we inform about the invalidity of approximation (i) of geostrophy for a reliable inference of the unapproximated *EPW*. We first evaluate the mesoscale *EKE* sources and sinks represented by the unapproximated *EPW*. We then characterize the main contributions to the unapproximated *EPW*.

5.1. Mesoscale *EKE* Sources and Sinks From the η-Based $EPW_{(i)}$ and the Unapproximated *EPW*

$EPW_{(i)}$ and *EPW* show no similarity over the whole Agulhas Current region (Figures 2a and 2d). In the WB region, they have similar patterns of locally opposite signs. These local differences are reflected in their cumulative values, which amount to an *EKE* sink (<0) and an *EKE* source (>0), for $EPW_{(i)}$ and *EPW* respectively. This confirms that approximation (i) of geostrophy is not valid for inferring *EPW* in the Agulhas Current region (Figures 2a and 2d).

The unapproximated *EPW* indicates a source of *EKE* in the WB region (0.82 GW; Figure 2d). The locally gained *EKE* is then exported downstream of the Agulhas Current, eventually toward the South Atlantic, or recirculated into the Indian Ocean along the Agulhas Return Current (vector field in Figure 2d). Locally, the unapproximated *EPW* shows patterns and magnitudes consistent with the documented variability of the Agulhas Current (Lutjeharms, 2006; Tedesco et al., 2022).

Along the northern branch of the WB region (31°–26°E), where the Agulhas Current is stable, the unapproximated *EPW* is weak compared to the rest of the domain and have patterns of contrasting sign (Figure 2d). *EPW* is negative upstream of the Natal Bight (31°E) and between the Natal Bight and the Agulhas Bank over a narrow band along the straight part of the shelf (26°−30.5°E). In these areas, *EPW* (<0) therefore indicates that the eddy dynamics are mainly acting to deplete the mesoscale reservoir. This is consistent with the northern Agulhas Current being stable due to the topographic constraint (Lutjeharms, 2006; Tedesco et al., 2022). *EPW* is locally positive at the Natal Bight. This is consistent with the punctual generation (4–5 times per year) of Natal Pulses: mesoscale eddies that are the main source of variability of the Northern Agulhas Current (Elipot & Beal, 2015; Lutjeharms, 2006).

Along the southern branch of the WB region (26°–23°E), where the shelf curvature increases and the Agulhas Current is unstable, the mesoscale *EPW* is large and positive (Figure 2d). In this area, *EPW* shows the largest *EKE* source of the WB region. This shows that eddy dynamics are mainly energizing the mesoscale reservoir there. This is consistent with the highly unstable nature of the southern Agulhas Current and the documented generation of quasi-permanent meanders there (Lutjeharms, Boebel, & Rossby, 2003; Lutjeharms, Penven, & Roy, 2003; Schubert et al., 2021). Note that the mesoscale *EPW* locally changes sign and becomes negative at the tip of the shelf (24°–23°E). There, the shelf curvature decreases and the current is constrained by the topography, locally enhancing *EKE* dissipation and preventing mixed barotropic-baroclinic instability to trigger (energy conversion terms of barotropic and baroclinic instability are negative, indicating a kinetic energy loss from mesoscale eddies in favor of the mean circulation; Tedesco et al., 2022).

5.2. Main Contributions to the Unapproximated *EPW*

Geostrophic effects are not the leading contribution to *EPW* in the Agulhas Current region. We therefore characterize the main contributions to the unapproximated mesoscale *EPW* below. We first evaluate the main contributions to the unapproximated *EPW* and then discuss their range of validity.

5.2.1. Contributions of Ageostrophic and Topographic Effects

The unapproximated *EPW* ($A + B + C$; Table 1; Figure 2d) consists of an *EKE* flux contribution ($A + B$; Figure 2b) and a topographic contribution (C; Figure 2c). Both are large and largely compensate in the Agulhas Current region. In the WB region, the cumulative value of *EPW* is dominated by the positive *EKE* flux contribution ($A + B$). However, it can be locally dominated by the negative topographic contribution (C), as for example, along the straight part of the shelf, where a narrow band of negative *EPW* is visible (30.5°E–26°E; Figure 2d).

The *EKE* flux contribution ($A + B$) and the topographic contribution (C) do not account for geostrophic and ageostrophic effects to the same extent. Approximation (i) of geostrophy limits the estimate of the *EKE* flux contribution ($A + B$), because the unapproximated $A + B$ (Figure 2e) is very different from its geostrophic analog ($A1$; Figure 2c). The velocity divergence contribution to the *EKE* flux (A) accounts for ageostrophic effects and the β-effect. While the eddy pressure shear work (B) exclusively accounts for ageostrophic effects (cf., Section 2.2.2). The geostrophic *EKE* flux is thus reduced to a linear β-effect ($A1$; Figure 2c), which we have shown to be negligible for the η-based $EPW_{(i)}$ ($A1 + A2 + C$; Figure 2a).

On the other hand, approximation (i) of geostrophy allows to derive a qualitatively good estimate of the topographic contribution (C). The unapproximated C-contribution (Figure 2f) is similar to the η-based $EPW_{(i)}$ ($A1 + A2 + C$; Figure 2a), which we have seen to be dominated by the geostrophic C-contribution (cf., Section 4).

Note that the EKE source shown by the unapproximated EPW in the WB region (0.82 GW; Figure 2d) is mainly due to the barotropic EPW (1.56 GW; not shown), while the first baroclinic EPW represents an EKE sink (−0.74 GW; not shown) and acts against the barotropic EPW. This emphasizes the importance of properly defining the unapproximated mesoscale EPW as the sum of barotropic and first baroclinic EPWs. In the case of the unapproximated EPW, both vertical modes compensate each other, while in the case of the η-based $EPW_{(i)}$, both vertical modes amplify each other (cf., Section 4). The different contributions of barotropic and first baroclinic modes to the different versions of EPW is therefore non-trivial.

In summary, the η-based $EPW_{(i)}$ and the unapproximated EPW support opposite paradigms in the Agulhas Current region, because they have different leading order contributions. We first showed that the η-based $EPW_{(i)}$ is dominated by the topographic contribution acting on the geostrophic EKE flux. We then showed that the unapproximated EPW is dominated overall by ageostrophic effects and locally by the topographic contribution. In the following section, we characterize the range of validity for the dominance of ageostrophic effects.

5.2.2. Scale Analysis Argument for Large Ageostrophic Effects and Weak β-Effect

5.2.2.1. Definition of a Cross-Over Scale

The founding hypothesis of the paradigm of mesoscale eddies graveyard at western boundaries was that long baroclinic Rossby waves are the main contributor to the EKE flux divergence (Zhai et al., 2010). This hypothesis favors one contribution of EPW—the β-effect ($A1$ in $EPW_{(i)}$; Table 1)—over others, which include ageostrophic effects and the topographic contribution. We have seen that for the EKE flux contribution ($A + B$) acting on the unapproximated EPW (Table 1), ageostrophic effects overcome the β-effect in the WB region of the Agulhas Current (cf., Section 5). Here, we use a scale analysis to evaluate in which regimes we can expect ageostrophic effects to dominate over the β-effect for the unapproximated EPW.

Ageostrophic effects acting on the EKE flux contribution ($A + B$; Table 1) take the form either of (a) both ageostrophic velocities and pressure ($EPW_{(ag)}$) or (b) coupled ageostrophic velocities to geostrophic pressure ($EPW_{(g,ag)}$). Using quasi-geostrophic scalings of velocity and pressure, we perform the scaling of $EPW_{(ag)}$ (Equation 11), $EPW_{(g,ag)}$ (Equation 12), and of the β-effect (Equation 13), as follows:

$$\left|\int_{-H}^{\eta} \nabla_H \cdot \left(\mathbf{u}'_{ag,n} p'_{ag,n} \phi_n^2\right)\, dz\right| \sim \frac{Ro^2 U'_g P'_g H}{L} \tag{11}$$

$$\left|\int_{-H}^{\eta} \nabla_H \cdot \left(\mathbf{u}'_{ag,n} p'_{g,n} \phi_n^2\right)\, dz\right| \sim \frac{Ro U'_g P'_g H}{L} \tag{12}$$

$$\left|\frac{\beta \rho_0 g^2}{2f^2} \int_{H}^{\eta} \frac{\partial}{\partial x}\left(\frac{\phi_n^2}{|\phi_n^2|_{z=0}} \alpha_n^2 \eta'^2\right) dz\right| \sim \frac{\hat{\beta} P' U'_g H}{\hat{f}} \tag{13}$$

We use the following adimensionalized variables $\left|\nabla_H, \frac{\partial}{\partial x}\right| \sim \frac{1}{L}$, $\left|\int_{-H}^{\eta} <.> dz\right| \sim H$, $|\beta| \sim \hat{\beta}$, $|f| \sim \hat{f}$. Using the expansion of velocity and eddy pressure with Ro the small parameter, we define $|\mathbf{u}'_{ag,n}| \sim RoU'_g$ and $\left|p'_{ag,n}\right| \sim RoP'_g$, with $Ro = \left|\frac{1}{H}\int_{-H}^{\eta}\left(\frac{\zeta'_{RMS}}{f}\right) dz\right| \sim \frac{\widehat{\zeta'_{RMS}}}{\hat{f}}$ the vertical average of the root mean square of the normalized relative vorticity for mesoscale eddies $\left(\zeta' = \partial xv' - \partial yu'\right)$. Using geostrophy, we define $|p'_{g,n}| \sim P'_g \sim \rho_0 \hat{f} U'_g L$. Using the hydrostatic approximation and geostrophy, we define $\left|\frac{\phi_n^2 \alpha_n^2 \eta'^2}{|\phi_n^2|_{z=0}}\right| \sim \frac{P'_g U'_g L\hat{f}}{\rho_0 g^2}$.

The scale analysis is used to define two cross-over scales ($L_{g,ag}$ in Equation 15 and L_{ag} in Equation 14), at which the contributions to EPW of the two forms of ageostrophic EKE flux ($EPW_{(g,ag)}$ and $EPW_{(ag)}$) have the same order of magnitude as the contribution of the β-effect:

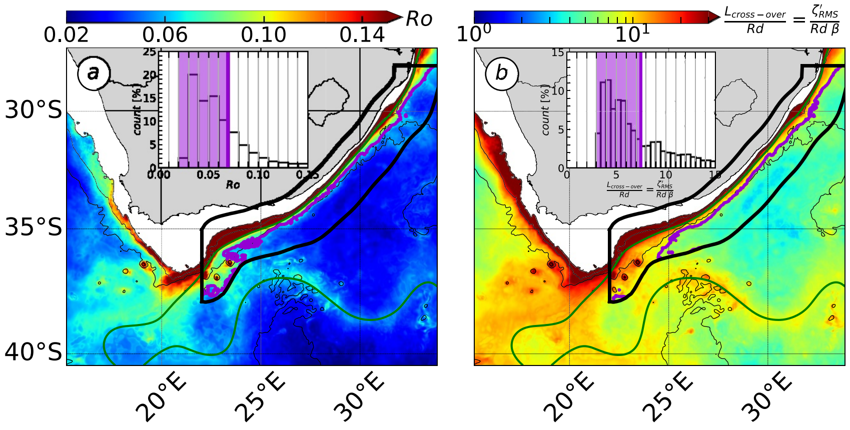

Figure 3. Adimensional metrics measuring the contribution of ageostrophic effects to *EPW*. (a) Rossby number for mesoscale eddies $\left(Ro = \frac{\zeta_{RMS}}{f}\right)$ and (b) ratio between the cross-over scale ($L_{g,ag} = \frac{\zeta_{RMS}}{\beta}$; Equation 15) and the characteristics length scale of mesoscale eddies (Rossby deformation radius; *Rd*). In the barplots, counts of (a) and (b) in the western boundary region are expressed in [%] and shaded areas show the 70% percentile. In the maps, purple contours show (a) and (b) 70% percentiles in the physical space. (cf., Figure 1 for a detailed caption).

$$\frac{(11)}{(13)} = \frac{Ro^2 \hat{f}}{L\hat{\beta}} = \frac{\widehat{\zeta'_{RMS}}^{\,2}}{L\hat{f}\hat{\beta}} = \frac{L_{ag}}{L}, \text{ with } L_{ag} = \frac{\widehat{\zeta'_{RMS}}^{\,2}}{\hat{f}\hat{\beta}} \tag{14}$$

$$\frac{(12)}{(13)} = \frac{Ro\hat{f}}{L\hat{\beta}} = \frac{\widehat{\zeta'_{RMS}}}{L\hat{\beta}} = \frac{L_{g,ag}}{L}, \text{ with } L_{g,ag} = \frac{\widehat{\zeta'_{RMS}}}{\hat{\beta}} \tag{15}$$

$L_{g,ag}$ is the ratio of the eddy vorticity and of the β parameter (Equation 15). $L_{g,ag}$ is greater than L_{ag} if the eddy Rossby number is <1, which is the case for mesoscale eddies. $L_{g,ag}$ will thus generally impose the most restrictive condition. Note that the definition of the cross-over scales is not unique. An equivalent definition involving the Rhines scale can be defined using another scaling of the eddy Rossby number$\left(Ro = \frac{U'}{fL}\right)$. See Appendix D for details on the alternative definition of $L_{g,ag}$ for the mesoscale *EPW* in the Agulhas Current region.

5.2.2.2. *Cross-Over Scale Performed in the Agulhas Current Region*

We compare $L_{g,ag}$ (Equation 15) with the characteristic length scale of mesoscale eddies—the Rossby deformation radius (*Rd*) of about 30 km in the region of the Agulhas Current—(Figure 3). The typical values of *Ro* confirm that mesoscale eddies are mainly geostrophic in the WB region (*Ro* in O(0.02–0.07) in 70% of the WB region and *Ro* in O(0.07–0.65) at the inner front; Figure 3a). However, the typical values of $L_{g,ag}$ show that coupled geostrophic-ageostrophic effects dominate over the β-effect at mesoscale ($L_{g,ag}$ in O(3–7)*Rd* in 70% of the WB region and $L_{g,ag}$ in O(7–19)*Rd* at the inner front; Figure 3b). On the other hand, the purely ageostrophic effects are weaker than the contribution of the β-effect (L_{ag} in O(0.1–0.5)*Rd* in the WB region; not shown).

Typical values of $L_{g,ag}$ (Equation 15) are about O(105–256) km in the region of the Agulhas Current (not shown). This sets the upper limit of the scale range where coupled geostrophic-ageostrophic effects are expected to dominate over the β-effect. This scale range is consistent with the result of the idealized numerical simulations shown in Zhai et al. (2010), where an eddy of 500 km-diameter was used to illustrate the validity of the approximated η-based version of *EPW*.

In summary, approximation (i) of geostrophy is not valid to infer the unapproximated *EPW* in the Agulhas Current region, because the coupled geostrophic-ageostrophic *EKE* flux overall dominate the *EPW* at the mesoscale range (105 km > L > *Rd* ~ 30 km). We evaluate in the next section, the use of approximation (i) of geostrophy to infer *AEKE* (Table 2), the nonlinear component of *EKE* flux divergence.

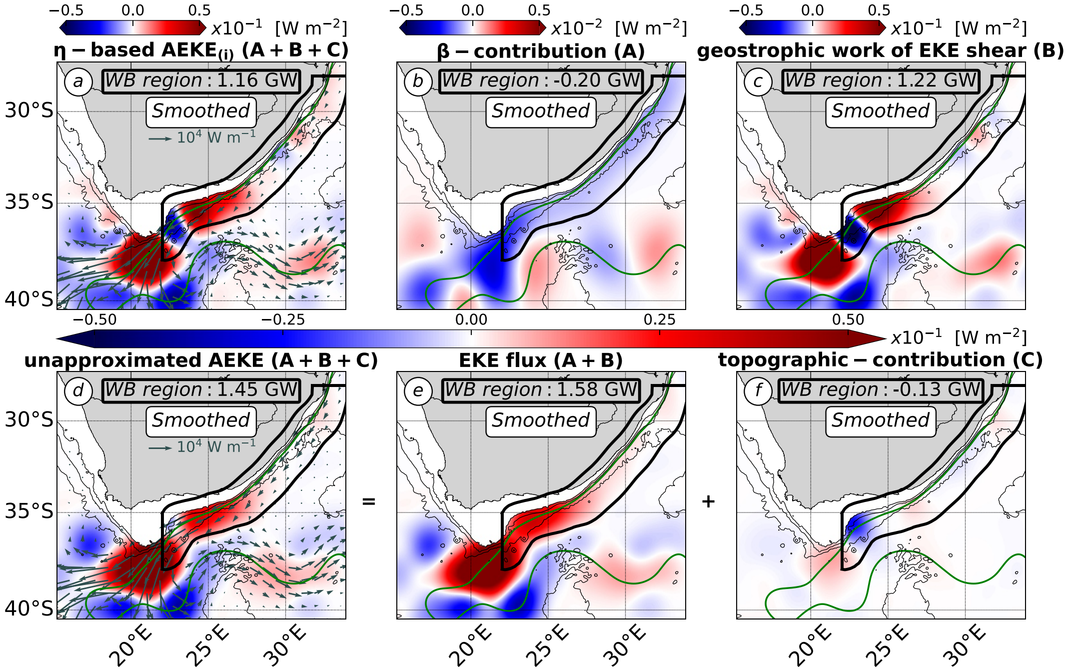

Figure 4. η-based $AEKE_{(i)}$ and unapproximated $AEKE$ [W m^{-2}] (Table 2). (a) η-based $AEKE_{(i)}$ $(A + B + C)$ split into the contributions of (b) β-effect (A) and (c) work of EKE shear (B). (d) Unapproximated $AEKE$ $(A + B + C)$ split into the contributions of (e) EKE flux $(A + B)$ and (f) topographic-contribution (C). (a,d) Vector fields show (a) geostrophic EKE flux $\left(\frac{\rho_0}{2}\int_{-H}^{\eta}\mathbf{u}_{g,n}\phi_n\|\mathbf{u}'_{g,n}\phi_n\|^2\,dz\right.$, with $n = 0 - 1$) and (d) unapproximated EKE flux $\left(\frac{\rho_0}{2}\int_{-H}^{\eta}\mathbf{u}_n\phi_n\|\mathbf{u}'_n\phi_n\|^2\,dz\right.$, with $n = 0 - 1$) [W m^{-1}]. Note the different colorbar ranges between (b) and the other panels. All terms are smoothed with a 75 km-radius Gaussian kernel. (cf., Figure 1 for a detailed caption).

6. η-Based $AEKE_{(i)}$ and Unapproximated $AEKE$

We first evaluate the mesoscale EKE sources and sinks represented by the η-based and the unapproximated $AEKE$. We then characterize the main contributions of the two $AEKE$s.

6.1. Mesoscale EKE Sources and Sinks From the η-Based $AEKE_{(i)}$ and the Unapproximated $AEKE$

Figures 4a and 4d shows the η-based $AEKE_{(i)}$ and unapproximated $AEKE$ in the Agulhas Current region. In the WB region, $AEKE_{(i)}$ and $AEKE$ are in fairly good agreement. Both $AEKE$s show a net EKE source (>0; Figures 4a and 4d). The η-based $AEKE_{(i)}$ accounts for 73% of the cumulative EKE source shown by the unapproximated $AEKE$ (the remaining 27% being accounted for by ageostrophic effects). The locally gained EKE is then exported out of the WB region, eventually into the South Atlantic Ocean or recirculated in the South Indian Ocean (vector field in Figures 4a and 4d). The large similarities between $AEKE_{(i)}$ and $AEKE$ indicate that approximation (i) of geostrophy is valid for qualitatively inferring $AEKE$.

The two $AEKE$s show patterns and magnitudes consistent with the documented variability of the Agulhas Current (Lutjeharms, 2006; Tedesco et al., 2022). Along the northern branch of the WB region (31°E–26°E), where the Agulhas Current is stable, both $AEKE$s are weak (one order of magnitude smaller than in the rest of the domain; Figures 4a and 4d). Along the southern branch of the WB region (26°–23°E), both $AEKE$s are large and generally positive where the shelf curvature increases and the current is documented to be unstable (Lutjeharms, 2006; Tedesco et al., 2022) (Figures 4a and 4d). In this area, the $AEKE$s indicate that the eddy dynamics mainly act to energize the mesoscale reservoir, similar to the unapproximated EPW (Figure 2d). Note that $AEKE_{(i)}$, and $AEKE$ in a lesser extend, locally change sign and becomes negative at the tip of the shelf (24°–23°E), where the topographic constraint on the current is large. This local magnitude difference between the EKE sinks shown by $AEKE_{(i)}$ and $AEKE$ suggests that ageostrophic effects substantially contribute to the mesoscale eddy dynamics at this location.

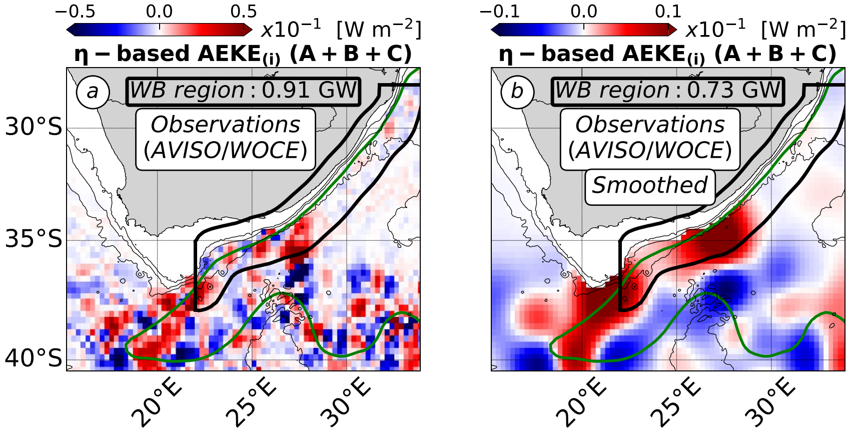

Figure 5. Observed η-based $AEKE_{(i)}$ [W m^{-2}] (Table 2). (a) Unsmoothed and (b) smoothed version of the observed η-based $AEKE_{(i)}$ performed using a combination of satellite altimetry data (AVISO), climatological data (WOCE) and model-based parameter (Equations 7 and 8). For (b), the smoothing radius is 75 km as for Figures 2 and 4. Note the different colorbar range between the two panels. (cf., Figure 1 for a detailed caption).

6.2. Main Contributions to the η-Based $AEKE_{(i)}$

The η-based $AEKE_{(i)}$ ($A + B + C$; Table 2; Figure 4a) consists of a geostrophic *EKE* flux contribution ($A + B$; Figures 4b and 4c) and a topographic contribution acting on the geostrophic *EKE* flux (C; not shown), which are of different importance in the Agulhas Current region. The geostrophic $A + B$-contribution accounts for 61% of the net $AEKE_{(i)}$, while the geostrophic topographic contribution accounts for the remaining 39%. Within the geostrophic *EKE* flux ($A + B$), the geostrophic *EKE* shear work (B) is the main contribution (Figure 4c). The geostrophic *EKE* shear work (B; Figure 4c) has locally similar patterns and magnitudes than $AEKE_{(i)}$ ($A + B + C$; Figure 4a) in the Agulhas Current region. The velocity divergence contribution (A) corresponds to a negligible nonlinear β-effect (Figure 4b). It represents a weak *EKE* sink in the WB region (<0; Figure 4b), similar to its linear analog acting on $EPW_{(i)}$ (A1; Figure 2c). In a nutshell, the η-based $AEKE_{(i)}$ ($A + B + C$; Table 2) is dominated by geostrophic effects in the form of the *EKE* shear work (B).

6.3. Main Contributions to the Unapproximated *AEKE*

Similar to the η-based $AEKE_{(i)}$, the unapproximated *AEKE* ($A + B + C$; Table 2) consists in an *EKE* flux contribution ($A + B$) and a topographic contribution (C), which are of different importance in the Agulhas Current region. In the WB region, *AEKE* ($A + B + C$; Figure 4d) is overall dominated by the positive *EKE* flux contribution ($A + B$; Figure 4e), except at the shelf tip (24°E–23°E) where it is locally dominated by the negative topographic contribution (C; Figure 4f).

The *EKE* flux contribution ($A + B$) and the topographic contribution (C) do not account for geostrophic and ageostrophic effects in the same proportions. Approximation (i) of geostrophy allows to infer a qualitative estimate of the patterns of the *EKE* flux contribution ($A + B$; the leading order contribution of $AEKE = A + B + C$). However, note that the ageostrophic effects acting on A and B are significant. The geostrophic *EKE* flux ($A + B$; Figures 4b and 4c) underestimates the *EKE* source shown by the unapproximated analog ($A + B$; Figure 4e) (underestimation of 35%).

On the other hand, approximation (i) of geostrophy limits the estimation of the patterns and magnitude of the topographic contribution (C; a secondary contribution to $AEKE = A + B + C$). Geostrophic and unapproximated C-contributions have cumulative values of opposite sign in the WB region (geostrophic C: 0.65 GW, not shown and unapproximated C: −0.38 GW in Figure 4f). This indicates that the topographic contribution (C) acting on *AEKE* is largely influenced by ageostrophic effects.

Note that the *EKE* source shown by the unapproximated *AEKE* (2.29 GW; Figure 4d) is due to the accumulation of the barotropic *AEKE* (0.79 GW; not shown) and first baroclinic *AEKE* (1.50 GW; not shown). This suggests that the mesoscale *AEKE* could be approximated from the contribution of the first baroclinic mode. Similar contributions of the barotropic and first baroclinic modes are found for the η-based $AEKE_{(i)}$ (mesoscale $AEKE_{(i)}$: 1.67 GW in Figure 4a and barotropic $AEKE_{(i)}$: 0.57 GW and first baroclinic $AEKE_{(i)}$: 1.10 GW; not shown).

In summary, the η-based $AEKE_{(i)}$ and the unapproximated $AEKE$ support similar paradigms in the Agulhas Current region, because geostrophic effects are a major contributor to $AEKE$ (via the EKE shear work B). However, the accurate estimation of its magnitude using η is less reliable. Indeed, ageostrophic effects also make a significant contribution to $AEKE$ ($A + B + C$), via all its sub-contributions (A, B, and C).

7. Summary and Discussion

In this study, we have investigated the main contributions to the mesoscale EKE flux divergence in the Agulhas Current region. Motivated by opposing η-based and model-based paradigms of mesoscale eddy dynamics, we aimed to evaluate the validity of the approximation (i) of geostrophy to infer the mesoscale EKE flux divergence in this region. Geostrophy is a good approximation for inferring mesoscale eddy velocities, but it is a different matter to use it to infer the EKE flux divergence (a tendency term of the EKE budget representing net EKE sources and sinks for ocean dynamics in equilibrium; Harrison & Robinson, 1978). Our analysis used a regional numerical simulation to evaluate the main contributions of the components of the EKE flux divergence, consisting of the EPW and the advection of EKE ($AEKE$). In this section, we summarize our main findings and discuss their implications for the understanding of mesoscale eddy dynamics.

7.1. On the Use of Sea Surface Height (η) to Infer the Mesoscale *EKE* Flux Divergence

7.1.1. Eddy Pressure Work (*EPW*)

Based on an approximate calculation of EPW using sea surface height (η), Zhai et al. (2010) showed that western boundaries are mesoscale EKE sinks. The η-based diagnosis of EPW is by definition geostrophic. It reduces to the contribution of long baroclinic Rossby waves (linear β-contribution acting on the first baroclinic mode) with additional approximations to (ii) the vertical structures of mesoscale eddies and (iii) the contribution of topography. Our results show that none of the approximations (i), (ii) and (iii) are valid to infer the mesoscale EPW in the Agulhas Current region.

We first showed that the η-based $EPW_{(i)}$ (considering only approximation (i); Table 1) is dominated by a topographic contribution acting on the barotropic and first baroclinic modes (Figures 2a–2d). While the Rossby waves contribution is negligible ($A1$; Figure 2c). This invalidates the use of approximations (ii) and (iii). We then showed that the unapproximated EPW (Table 1) is dominated overall by the coupled geostrophic-ageostrophic EKE flux and locally by topographic interactions (Figures 2d–2f and 3b). A scale analysis emphasized that the coupled geostrophic-ageostrophic EKE flux dominates EPW at mesoscale ($L > O(30)$ km), while the β-effect could potentially dominate EPW at larger scales ($L > O(105–256)$ km).

The dominance of ageostrophic effects explains the opposite paradigms supported by the η-based $EPW_{(i)}$ and the unapproximated EPW in the Agulhas Current region. This also invalidates the use of approximation (i) of geostrophy to infer the mesoscale EPW in this region.

7.1.2. Advection of Eddy Kinetic Energy (*AEKE*)

We have defined and performed an unapproximated η-based version of the $AEKE$ component ($AEKE_{(i)}$; Table 2) in the Agulhas Current region. Our results show that approximation (i) of geostrophy is valid to infer a qualitative mesoscale $AEKE$. Unapproximated $AEKE$ and η-based $AEKE_{(i)}$ support similar paradigms in the Agulhas Current region (Figures 4a and 4d), because geostrophic effects largely contribute to $AEKE$ ($A + B + C$; Figure 4a), via the term of the EKE shear work (B; Figure 4c).

Our results support the use of η to qualitatively infer the mesoscale EKE source represented by the $AEKE$ component in the WB region of the Agulhas Current. This is furtherly supported by the η-based $AEKE_{(i)}$ performed using observations (Figure 5). The observed η-based $AEKE_{(i)}$ (Table 2) is calculated by combining: (a) η measured by satellite altimetry, (b) vertical modes calculated from time-averaged stratification derived from the WOCE climatology, and (c) $\lambda_n = \frac{\eta_n}{\eta}$ (Section 2.3.1) and $\alpha_n = \frac{\eta_{n_t}}{\eta_t}$ (Section 2.3.1) parameters—modulating η according to vertical modes—derived from our numerical simulation at each time step and spatially averaged over the WB region. The observed η-based $AEKE_{(i)}$ shows a mesoscale EKE source in the WB region in fairly good agreement with the modeled η-based $AEKE_{(i)}$ and the modeled unapproximated $AEKE$ (Figures 4a, 4d, and 5a). It shows a large EKE source extending from about 26°E to the Retroflection (20°E), whose cumulative value is 43% and 32% of that of the modeled η-based $AEKE_{(i)}$ and the unapproximated $AEKE$, respectively.

Note that the fairly good qualitative agreement between observed η-based $AEKE$ and modeled versions of $AEKE$ (Figures 4a, 4d, and 5a) highlights a reliable alternative to approximation (ii). The contribution of the barotropic and first baroclinic modes to η, and hence to $AEKE$, can be reliably approximated in small regions using spatially averaged model-based partitioning of the modal η.

7.1.3. Conclusion on the Mesoscale *EKE* Flux Divergence (*EPW* and *AEKE*)

Our thorough analysis of the contributions to EPW and $AEKE$ (forming the EKE flux divergence) allows us to conclude on the use of η to infer mesoscale EKE sources and sinks in the Agulhas Current region. $AEKE$ represents the larger cumulative contribution ($AEKE$: 2.29 GW) to the EKE flux divergence in the WB region ($EPW + AEKE$: 3.12 GW; Figures 2d and 4d). Although, the approximation of geostrophy (i) does not allow to infer EPW (Figures 2a and 2d), it does allow to infer a qualitative estimate of $AEKE$ (73%; Figures 4a and 4d). This indicates that a qualitative estimate of the EKE flux divergence can be inferred from η, via the $AEKE$ component. In the model, using the η-based $AEKE_{(i)}$ as a proxy for the EKE flux divergence would lead to an underestimation of 46% of the EKE source in the WB region of the Agulhas Current (Figures 4a and 4d). From observations, however, the underestimation appears to be significantly larger (76%; Figures 4d and 5b). Further investigation would therefore be required to conclude on the use of η measured by satellite altimetry to reliably infer the magnitude of the EKE source in this region.

Our results support the use of η to infer a qualitative estimate of the mesoscale $AEKE$, and subsequently of the mesoscale EKE flux divergence, but for fundamentally different reasons than Zhai et al. (2010). Zhai et al. (2010) used approximation (i) of geostrophy based on the hypothesis that long baroclinic Rossby waves are the main contributor to the EKE flux divergence. We show in this study that geostrophic effects make a significant contribution to the EKE flux divergence in the Agulhas Current region, via the advection of geostrophic EKE by geostrophic mean and eddy flows ($AEKE$).

7.2. On the Mesoscale Eddy Energy Budget at Western Boundaries

7.2.1. Main Contributions Acting on the Mesoscale *EKE* Flux Divergence

The paradigm of a mesoscale eddies graveyard at western boundaries supported by Zhai et al. (2010) relies on long baroclinic Rossby waves (β-effect) as the main contributor to the mesoscale EKE flux divergence. Our results suggest that the mesoscale EKE flux divergence may not be dominated by the β-effect in WB regions.

Our scaling analysis showed that the magnitude of the linear β-contribution to EPW depends on metrics that provide a measure of dynamical and regional characteristics (Ro: mesoscale eddy Rossby number and the β parameter, respectively). The β parameter is usually low compared to Ro at mid-latitudes, resulting in a weak β-contribution to EPW. However, the β parameter is larger at low latitudes, suggesting that these regions may be more conducive to a large linear β-contribution to the EKE flux divergence. However, topographic interactions are large at western boundaries regardless of latitude. The topographic contribution may therefore be as large or larger than the β-effect contribution to the EKE flux divergence at western boundaries of all latitudes.

7.2.2. Main Sources and Sinks of *EKE*

The positive EKE flux divergence indicates that the mesoscale eddy dynamics in the WB region of the Agulhas Current are locally dominated by processes energizing the mesoscale EKE reservoir. A recent study characterized the processes contributing to the mesoscale EKE source in this region (Tedesco et al., 2022). They showed that the local generation of mesoscale eddies—due to barotropic and mixed barotropic-baroclinic instabilities of the Agulhas Current—overcomes the local decay of locally- and remotely generated mesoscale eddies—mainly due to bottom stress and topographically channeled processes. Our current study complements the process study of Tedesco et al. (2022), by showing (a) that the local mesoscale EKE source is largely redistributed in space by the advection done by geostrophic mean and eddy flows and (b) that this net spatial redistribution can be qualitatively inferred from η fields.

We suggest that the *EKE* flux divergence at western boundaries may vary with the presence or absence of a WB current. However, additional studies of other WB regions—with or without a WB current and for a broad latitudinal range—would be required to draw conclusions about the mesoscale eddy dynamics at each WB. The mesoscale *EKE* flux divergence could represent an *EKE* sink in the WB regions without a WB current, as topographically channeled processes damping mesoscale eddies would locally dominate. This is supported by studies based on in situ observations and idealized numerical simulations, for WB regions without a WB current (Evans et al., 2020, 2022; Z. Yang et al., 2021). The mesoscale *EKE* flux divergence could represent an *EKE* source in WB regions with a WB current, as the local generation of mesoscale eddies would dominate the damping effect of topographic interactions, similar to the Agulhas Current region (Tedesco et al., 2022). This is supported by the intense generation of mesoscale eddies by flow instabilities documented in several WB currents (Gula et al., 2015; Halo et al., 2014; Jamet et al., 2021; Kang & Curchitser, 2015; Li et al., 2021; Tedesco et al., 2022; Yan et al., 2019; Y. Yang & Liang, 2016). Furthermore, an exhaustive description of the processes contributing to mesoscale eddy decay in WB regions including a WB current, should include eddy-mean interactions in addition to topographic interactions (Adcock & Marshall, 2000; Chen et al., 2014; Holloway, 1987; Tedesco et al., 2022).

Appendix A: Observed and Modeled Sea Surface Height (η) Variance in the Agulhas Current Region

The evaluation of the η-based version of the *EKE* flux divergence defined by Zhai et al. (2010) ($EPW_{(i,ii,iii)}$) in the model and observations, suggest that the modeled mesoscale eddy field might be weaker compared to observations (cf., Section 3.3). The model of horizontal resolution of dx $\sim$2.5 km, used in this study, is forced at the boundaries at each time step by a parent model of dx $\sim$7.5 km. The parent simulation resolve mesoscale eddies of scales 50–100 km, but may underestimate their magnitude due to a too weak inverse turbulent cascade at smaller scales. This process has been shown to be of importance in the Subgyre regions of the Agulhas Current system (Schubert et al., 2020).

Based on this assumption, we evaluate the modeled mesoscale variability (η variance) simulated by the parent simulation (dx $\sim$7.5 km) against satellite altimetry data (Figure A1). The parent simulation covers the western part of the subtropical gyre of the Indian Ocean. The Agulhas Current originates from the lower end of the Mozambique Channel (32.5°E), where it feeds upon the Mozambique Current and the East Madagascar Current. The Agulhas Current flows along the South African coastline to the South African tip (20°E). From there, it Retroflects and become the Agulhas Return Current flowing eastward into the South Indian Ocean.

Modeled η variance represents the variability of the Agulhas Current system in overall good agreement with observations. The Mozambique Current, the East Madagascar Current and the Agulhas Current show moderate

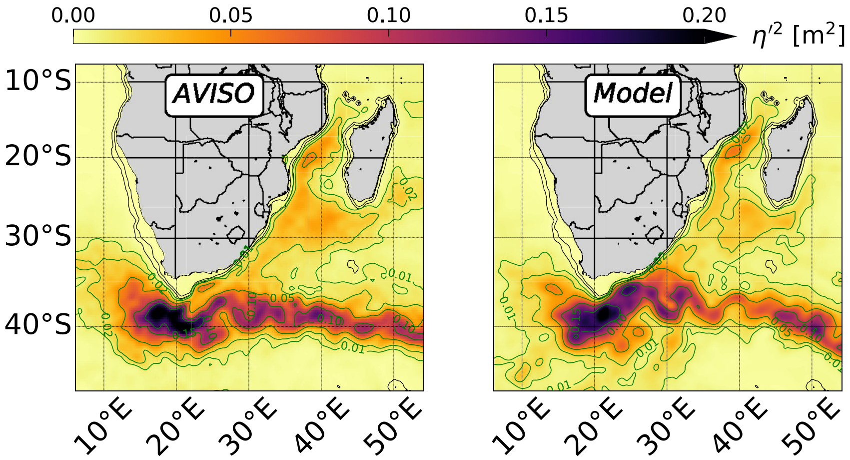

Figure A1. Observed and modeled mesoscale variability at the surface in the Agulhas Current system. η variance (η'^2) [m^2] performed from (a) satellite altimetry data (AVISO) and (b) a numerical simulation (dx $\sim$7.5 km). Green contours denote isolines of η variance and black contours denote 300 and 1,000 m isobaths.

value of η variance (O(0.02–0.03) m^2). The Agulhas Retroflection and the Agulhas Return Current show the largest η variance (O(0.05–0.15) m^2). In the context of our study, a relevant difference is the weaker modeled η variance in the Subgyre region (35°–45°E and 25°–35°S). There, the model shows moderate value of smaller extend than in observations. This confirms that the modeled mesoscale eddies propagating westward through the Subgyre toward the Agulhas Current region have a weaker amplitude than in observations. This supports the weaker amplitude of the *EKE* sink in the WB region shown by the modeled $EPW_{(i,ii,iii)}$compared to observed one, to be due to a weaker modeled mesoscale eddy field forced at the boundaries.

Appendix B: Sensitivity of the Unapproximated *EPW* to Spatial Smoothing

The unapproximated *EPW* (Table 1) is spatially smoothed to emphasize the large-scale patterns driving its cumulative contribution in the WB region (Figure B1). The unsmoothed *EPW* is characterized by small-scales patterns that are the most intense at topographic features—shelf slope (1,000 m isobath), seamounts, canyons, roughness, among others—locally peaking at O(2.5–10) W m^{-2} (Figure B1a). In the WB region, the intense small-scales patterns of the unapproximated *EPW* are larger by one or two order of magnitude than the unsmoothed $EPW_{(i,ii,iii)}$ (O(0.01) W m^{-2}; Figure 2a). However, the magnitude of the cumulative contribution of *EPW* (1.31 GW; Figure B1a) is close to the one of $EPW_{(i,ii,iii)}$ (−1.32 GW; Figure 1b) in this region, regardless of the intense small-scale patterns. It indicates that the intense small-scale patterns locally compensate and do not significantly contribute to the cumulative *EPW* in the WB region.

The sensitivity of the unapproximated *EPW* to the smoothing is shown using a Gaussian kernel of progressively increasing length scale: from 35 km (the spatially-averaged Rossby deformation radius in region the modeled region) to 50 and 75 km (two typical mesoscale eddies radii at mid-latitudes; Chelton et al., 2011). The patterns of *EPW* change with the different smoothing length scales, but the order of magnitude of the cumulative contribution

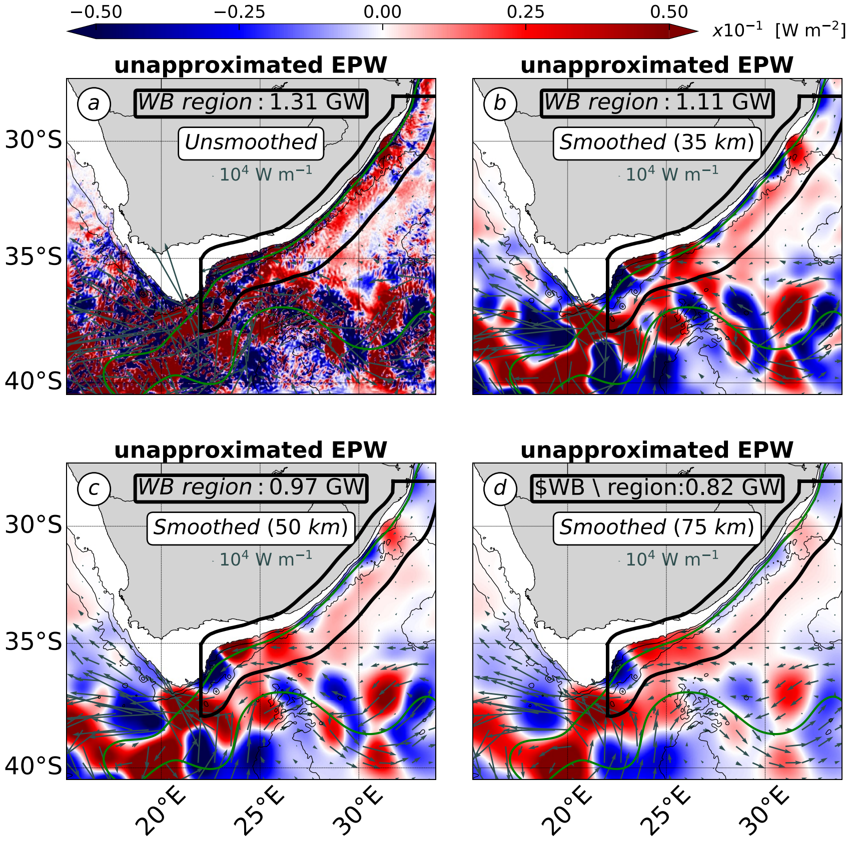

Figure B1. Sensitivity of the unapproximated *EPW* [W m^{-2}] (Table 1) to spatial smoothing. *EPW* shown for (a) no spatial smoothing and (b, c, and d) spatial smoothing of different radius from (b) 35 km, (c) 50 km to (d) 75 km. Vector fields show the corresponding smoothed *EKE* flux ($\int_{-H}^{\eta} \mathbf{u}'_n p'_n \phi_n^2 \, dz$, with $n = 0 - 1$) [W m^{-1}]. (cf., Figure 1 for a detailed caption).

in the WB region is reasonably unchanged ($\leq$30%; Figure B1). A similar sensitivity to the smoothing is found for the unapproximated *AEKE* ($\leq$20%; not shown).

In the study, the label 'smoothed' in Figures refers to the Gaussian kernel using a 75 km-radius. The smoothings using 50 km- and 75 km-radius result in fairly close cumulative *EPW* in the WB region (Figures B1c and B1d). However, the 75 km-radius smoothing provides smoother patterns, emphasizing the most the large-scale patterns driving the *EPW* cumulative in the WB region, and facilitating the most its comparison with $EPW_{(i,ii,iii)}$ (Table 1; Figure 1b).

Appendix C: Partitioning of Sea Surface Height (η) Variance into the Barotropic and 9 First Baroclinic Vertical Modes

In order to assess the validity of approximations (ii) and (iii) to infer *EPW*, we progressively relax the use of the approximations when inferring the η-based *EPW* term (cf., Section 4). Relaxing the use of approximation (ii) of η primarily reflecting the first baroclinic mode, requires to evaluate the partitioning of the η variance into the different vertical modes ($\alpha_n^2 = \frac{\eta_n'^2}{\eta'^2}$; Equation 8 in Section 2.3.1). η is a two-dimensional field and cannot be straightforwardly projected onto the vertical mode base. However, the modal coefficient for η (η_n) can be inferred such as: $\eta_h = \frac{p_n'(z=0)}{\rho_0 g}$, using the modal pressure at $z = 0$ m and the hydrostatic relationship.

The modal expression of the η variance (η'^2) and α_n^2 are defined as follows:

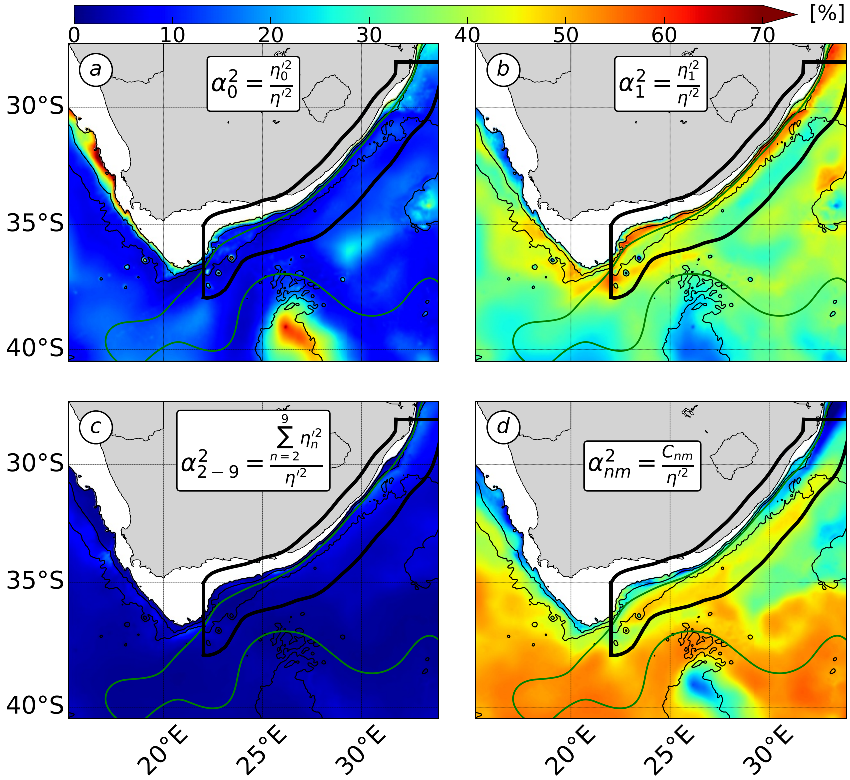

Figure C1. Partitioning of the sea surface height variance into categories of vertical modes $\left(\alpha_n^2 = \frac{\eta_n'^2}{\eta'^2}\right)$ [%], including (a) the barotropic mode ($n = 0$), (b) the first baroclinic mode ($n = 1$), (c) higher baroclinic modes ($n = 2 - 9$) and (d) the intermodal coupling at the surface (C_{nm}). (cf., Figure 1 for a detailed caption).

$$
\begin{aligned}
\eta'^2 &= \sum_{n=0}^{\infty} \eta'_n \sum_{m=0}^{\infty} \eta'_m \\
\eta'^2 &= \sum_{n=0}^{\infty} \eta'^2_n + \underbrace{\sum_{n=0}^{\infty} \sum_{m\neq n}^{\infty} \eta'_n \eta'_m}_{Intermodal\ coupling\ (C_{nm})} \\
\eta'^2 &= \sum_{n=0}^{\infty} \eta'^2_n + C_{nm}
\end{aligned}
\tag{C1}
$$

$$
\alpha_n^2 = \frac{\eta'^2_n}{\eta'^2} \text{ and } \alpha_{nm} = \frac{C_{nm}}{\eta'^2}
\tag{C2}
$$

The modal expression of the variance of η (Equation C1) involves an intermodal coupling term (C_{nm}). It corresponds to a phase-locked combination of vertical modes at the surface due to the modal correlation in time (Scott & Furnival, 2012; Wunsch, 1997). The degree of the surface modal correlation $\left(\frac{\sum_{n=0}^{9} \eta'^2_n}{\sum_{n=0}^{9} \eta'^2_n + C_{nm}}\right)$ is 1.8 in average in our numerical simulation, which is consistent with the 2–3 factor determined at global-scale from in situ data (Wunsch, 1997). However, it must be noted that the unapproximated *EPW* (Table 1) only accounts for the contribution of individual modes ($n = 0$ and $n = 1$). The coupling term C_{nm} is of importance for accurately decomposing η into vertical modes, but it does not contribute to the vertically-integrated form of the mesoscale *EKE* flux divergence considered in this study. Indeed, *EPW* involves the orthogonality condition resulting in canceling out the contribution of C_{nm} to *EPW*.

Using our numerical simulation of the Agulhas Current, we inferred α_n^2 the partitioning of the η variance into the barotropic and 9 first baroclinic modes (Figure C1). The barotropic and 10 first baroclinic modes account for 85%–100% of the modeled η variance in the region (not shown).

In the WB region, The η variance mainly partitions into the first baroclinic mode (38 ± 2%; Figure C1b) and C_{nm} the intermodal coupling term (36 ± 2%; Figure C1d). It partitions more weakly, but still significantly into the barotropic mode (16 ± 4%) (Figure C1a). This is partially consistent with the usual interpretation of η primarily reflecting the first baroclinic mode (Smith & Vallis, 2001; Wunsch, 1997). However, it also indicates that the vertical structure of mesoscale eddies—formally represented by the combination of the barotropic ($n = 0$) and first baroclinic modes ($n = 1$) (Smith & Vallis, 2001; Tedesco et al., 2022; Venaille et al., 2011; Wunsch, 2007)—can be accurately inferred from η field. This enables us to relax approximation (ii) and compute the unapproximated η-based $EPW_{(i)}$ (defined as the sum of the barotropic and first baroclinic contributions) from the modeled η field (cf., Section 4).

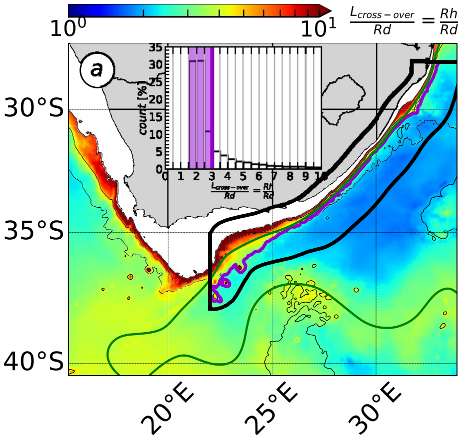

Figure D1. Alternative cross-over scale ($L_{g,ag} = Rh = \frac{1}{H}\int_{-H}^{\eta}\left(\sqrt{\frac{\|\mathbf{u}'\|}{\beta}}\right)dz$, with $\|\mathbf{u}'\|$ the magnitude of mesoscale eddies velocity) in the Agulhas Current region. (a) Ratio between the alternative cross-over scale and the characteristic length scale of mesoscale eddies (Rossby deformation radius; *Rd*). In the barplot, counts of (a) in the western boundary region are in [%] and shaded area shows the 70% percentile. In the map, purple contours show 70% percentile of (a) in the physical space. (cf., Figure 1 for a detailed caption).

Appendix D: Alternative Definition of the Cross-Over Scale Based on the Rhines Scale

Our scale analysis allows us to define a cross-over scale, marking the transition between regimes of large ageostrophic effects and large β-effect acting on the unapproximated *EPW* (cf., Section 5.2.2). Using quasi-geostrophic scalings for horizontal velocity and pressure, the cross-over scale is determined by the magnitude of the mesoscale eddies Rossby number (*Ro*) with respect to the β-parameter (Equation 15). The definition of the cross-over scale is not unique and changes with the scaling of *Ro*. Using $Ro = \frac{U'}{fL}$ (instead of $Ro = \zeta_{RMS} f$ in Section 5.2.2), we define an alternative cross-over scale, which corresponds to the Rhines scale ($Rh = \frac{1}{H}\int_{-H}^{\eta}\left(\sqrt{\frac{\|\mathbf{u}'\|}{\beta}}\right)dz$, with $\|\mathbf{u}'\|$ the magnitude of mesoscale eddies velocity). In the quasi-geostrophic theory, the Rhines scale marks the transition from an advectivelydominated (nonlinear) dynamical regime ($Rh \gg L$; with L the characteristic length scale of eddies) to a Rossby waves-dominated (linear) dynamical regime ($Rh \ll L$) (Rhines, 1975). This definition of the cross-over scale shows that evaluating the dominant regime of the mesoscale *EPW* is therefore similar to evaluating the mesoscale eddies dynamical regime.

In the Agulhas Current region, the typical values of the Rhines scale support the conclusions arising from the version of the cross-over scale presented in the study (Equation 15 and Figure 3b). The Rhines scale indicates that mesoscale eddies fall in the range of large coupled geostrophic-ageostrophic *EPW* with respect to the linear β-contribution (Rh in $O(1.5–3)Rd$ in 70% of the WB region and larger values at the inner front; Figure D1). This results shows that in the WB region of the Agulhas Current, mesoscale eddies fall in the range of large coupled geostrophic-ageostrophic flux—with respect to linear β-effect—as a result of mesoscale eddies being characterized by a nonlinear dynamical regime ($Rh \gg Rd$)—and not a linear wave dynamical regime ($Rh \ll L$). Nonlinear dynamics of mesoscale eddies has been characterized from satellite altimetry data, as documented by Chelton et al. (2011).

Data Availability Statement

WOES36 model outputs are available online at http://dap.saeon.ac.za/thredds/catalog/SAEON.EGAGASINI/2019.Penven/DAILY_MEANS/1_36_degree/catalog.html The AVISO data are available at www.aviso.altimetry.fr, the WOA18 and WOCE climatologies are available at www.nodc.noaa.gov/OC5/woa18/ and https://icdc.cen.uni-hamburg.de/thredds/catalog/ftpthredds/woce/catalog.htm.

Acknowledgments
This work was granted access to the HPC resources of IDRIS under the allocation A0040107630 made by GENCI at Paris, France, and of the HPC facilities DATARMOR of “Pôle de Calcul Intensif pour la Mer” at Ifremer, Brest, France. This work was supported by the Ifremer and the Brittany region for PhD funding. We also gratefully acknowledge support from the French National Agency for Research (ANR) through the projects DEEPER (ANR-19-CE01-0002-01) and the project DIEGO of the CNES/TOSCA SWOT program.

References

Adcock, S., & Marshall, D. (2000). Interactions between geostrophic eddies and the mean circulation over large-scale bottom topography. *Journal of Physical Oceanography*, *30*(12), 3223–3238. https://doi.org/10.1175/1520-0485(2000)030<3223:ibgeat>2.0.co;2

Capó, E., Orfila, A., Mason, E., & Ruiz, S. (2019). Energy conversion routes in the Western Mediterranean Sea estimated from eddy–mean flow interactions. *Journal of Physical Oceanography*, *49*(1), 247–267. https://doi.org/10.1175/jpo-d-18-0036.1

Chelton, D., Deszoeke, R., Schlax, M., El Naggar, K., & Siwertz, N. (1998). Geographical variability of the first baroclinic Rossby radius of deformation. *Journal of Physical Oceanography*, *28*(3), 433–460. https://doi.org/10.1175/1520-0485(1998)028<0433:gvotfb>2.0.co;2

Chelton, D., Schlax, M., & Samelson, R. (2011). Global observations of nonlinear mesoscale eddies. *Progress in Oceanography*, *91*(2), 167–216. https://doi.org/10.1016/j.pocean.2011.01.002

Chelton, D., Schlax, M., Samelson, R., & de Szoeke, R. (2007). Global observations of large oceanic eddies. *Geophysical Research Letters*, *34*(15), L15606. https://doi.org/10.1029/2007gl030812

Chen, R., Flierl, G., & Wunsch, C. (2014). A description of local and nonlocal eddy–mean flow interaction in a global eddy-permitting state estimate. *Journal of Physical Oceanography*, *44*(9), 2336–2352. https://doi.org/10.1175/jpo-d-14-0009.1

Cushman-Roisin, B., & Beckers, J.-M. (2011). *Introduction to geophysical fluid dynamics: Physical and numerical aspects*. Academic Press.

Debreu, L., Marchesiello, P., Penven, P., & Chambon, G. (2012). Two-way nesting in split-explicit ocean models: Algorithms, implementation and validation. *Ocean Modelling*, *49–50*, 1–21. https://doi.org/10.1016/j.ocemod.2012.03.003

Ducet, N., Traon, P.-Y. L., & Reverdin, G. (2000). Global high-resolution mapping of ocean circulation from TOPEX/Poseidon and ERS-1 and-2. *Journal of Geophysical Research*, *105*(C8), 19477–19498. https://doi.org/10.1029/2000jc900063

Elipot, S., & Beal, L. M. (2015). Characteristics, energetics, and origins of Agulhas Current Meanders and their limited influence on ring shedding. *Journal of Physical Oceanography*, *45*(9), 2294–2314. https://doi.org/10.1175/JPO-D-14-0254.1

Evans, D., Frajka-Williams, E., & Garabato, A. N. (2022). Dissipation of mesoscale eddies at a western boundary via a direct energy cascade. *Scientific Reports*, *12*(1), 1–13.

Evans, D., Frajka-Williams, E., Garabato, A. N., Polzin, K., & Forryan, A. (2020). Mesoscale eddy dissipation by a ‘zoo’ of submesoscale processes at a western boundary. *Journal of Geophysical Research: Oceans*, *125*(11), e2020JC016246. https://doi.org/10.1029/2020jc016246

Ferrari, R., & Wunsch, C. (2009). Ocean circulation kinetic energy: Reservoirs, sources, and sinks. *Annual Review of Fluid Mechanics*, *41*(1), 253–282. https://doi.org/10.1146/annurev.fluid.40.111406.102139

Gill, A. (1982). *Atmosphere-ocean dynamics*. *International Geophysics Series*. Academic Press.

Gill, A., Green, J., & Simmons, A. (1974). Energy partition in the large-scale ocean circulation and the production of mid-ocean eddies. *Deep-Sea Research and Oceanographic Abstracts*, *21*(7), 499–528. https://doi.org/10.1016/0011-7471(74)90010-2

Gouretski, V., & Koltermann, K. (2004). WOCE global hydrographic climatology. *Berichte des BSH*, *35*, 1–52.

Gula, J., Molemaker, M., & McWilliams, J. (2015). Gulf Stream dynamics along the Southeastern U.S. Seaboard. *Journal of Physical Oceanography*, *45*(3), 690–715. https://doi.org/10.1175/jpo-d-14-0154.1

Halo, I., Penven, P., Backeberg, B., Ansorge, I., Shillington, F., & Roman, R. (2014). Mesoscale eddy variability in the southern extension of the East Madagascar Current: Seasonal cycle, energy conversion terms, and eddy mean properties. *Journal of Geophysical Research: Oceans*, *119*(10), 7324–7356. https://doi.org/10.1002/2014jc009820

Harrison, D. E., & Robinson, A. R. (1978). Energy analysis of open regions of turbulent flows—Mean eddy energetics of a numerical ocean circulation experiment. *Dynamics of Atmospheres and Oceans*, *2*(2), 185–211. https://doi.org/10.1016/0377-0265(78)90009-x

Holloway, G. (1987). Systematic forcing of large-scale geophysical flows by eddy-topography interaction. *Journal of Fluid Mechanics*, *184*, 463–476. https://doi.org/10.1017/s0022112087002970

Jamet, Q., Deremble, B., Wienders, N., Uchida, T., & Dewar, W. (2021). On wind-driven energetics of subtropical gyres. *Journal of Advances in Modeling Earth Systems*, *13*(4), e2020MS002329. https://doi.org/10.1029/2020ms002329

Kang, D., & Curchitser, E. (2015). Energetics of eddy–mean flow interactions in the Gulf Stream region. *Journal of Physical Oceanography*, *45*(4), 1103–1120. https://doi.org/10.1175/jpo-d-14-0200.1

Kelly, S. (2016). The vertical mode decomposition of surface and internal tides in the presence of a free surface and arbitrary topography. *Journal of Physical Oceanography*, *46*(12), 3777–3788. https://doi.org/10.1175/jpo-d-16-0131.1

Kelly, S., Nash, J., & Kunze, E. (2010). Internal-tide energy over topography. *Journal of Geophysical Research*, *115*(C6), C06014. https://doi.org/10.1029/2009jc005618

Kelly, S., Nash, J., Martini, K., Alford, H. M., & Kunze, E. (2012). The cascade of tidal energy from low to high modes on a continental slope. *Journal of Physical Oceanography*, *42*(7), 1217–1232. https://doi.org/10.1175/jpo-d-11-0231.1

Li, J., Roughan, M., & Kerry, C. (2021). Dynamics of interannual eddy kinetic energy modulations in a western boundary current. *Geophysical Research Letters*, *48*(19), e2021GL094115. https://doi.org/10.1029/2021gl094115

Lutjeharms, J. (2006). *The Agulhas Current* (Vol. 2). Springer.

Lutjeharms, J., Boebel, O., & Rossby, H. (2003). Agulhas cyclones. *Deep Sea Research Part II: Topical Studies in Oceanography*, *50*(1), 13–34. https://doi.org/10.1016/s0967-0645(02)00378-8

Lutjeharms, J., Penven, P., & Roy, C. (2003). Modelling the shear edge eddies of the southern Agulhas Current. *Continental Shelf Research*, *23*(11–13), 1099–1115. https://doi.org/10.1016/s0278-4343(03)00106-7

Masuda, A. (1978). Group velocity and energy transport by Rossby waves. *Journal of Oceanography*, *34*(1), 1–7. https://doi.org/10.1007/bf02109610

Müller, P., McWilliams, J., & Molemaker, M. (2005). *Routes to dissipation in the ocean: The 2D/3D turbulence conundrum*. Cambridge University Press.

Nikurashin, M., & Ferrari, R. (2010). Radiation and dissipation of internal waves generated by geostrophic motions impinging on small-scale topography: Theory. *Journal of Physical Oceanography*, *40*(5), 1055–1074. https://doi.org/10.1175/2009jpo4199.1

Perfect, B., Kumar, N., & Riley, J. (2020). Energetics of seamount wakes. Part I: Energy exchange. *Journal of Physical Oceanography*, *50*(5), 1365–1382. https://doi.org/10.1175/jpo-d-19-0105.1

Rhines, P. (1975). Waves and turbulence on a beta-plane. *Journal of Fluid Mechanics*, *69*(3), 417–443. https://doi.org/10.1017/s0022112075001504

Schubert, R., Gula, J., & Biastoch, A. (2021). Submesoscale flows impact Agulhas leakage in ocean simulations. *Communications Earth & Environment*, *2*(1), 1–8. https://doi.org/10.1038/s43247-021-00271-y

Schubert, R., Gula, J., Greatbatch, R., Baschek, B., & Biastoch, A. (2020). The submesoscale kinetic energy cascade: Mesoscale absorption of submesoscale mixed layer eddies and frontal downscale fluxes. *Journal of Physical Oceanography*, *50*(9), 2573–2589. https://doi.org/10.1175/jpo-d-19-0311.1

Scott, R., & Furnival, D. (2012). Assessment of traditional and new eigenfunction bases applied to extrapolation of surface geostrophic current time series to below the surface in an idealized primitive equation simulation. *Journal of Physical Oceanography*, *42*(1), 165–178. https://doi.org/10.1175/2011jpo4523.1

Shchepetkin, A., & McWilliams, J. (2005). The Regional Oceanic Modeling System (ROMS): A split-explicit, free-surface, topography-following-coordinate ocean model. *Ocean Modelling*, *9*(4), 347–404. https://doi.org/10.1016/j.ocemod.2004.08.002

Smith, K., & Vallis, G. (2001). The scales and equilibration of midocean eddies: Freely evolving flow. *Journal of Physical Oceanography*, *31*(2), 554–571. https://doi.org/10.1175/1520-0485(2001)031<0554:tsaeom>2.0.co;2

Soufflet, Y., Marchesiello, P., Lemarié, F., Jouanno, J., Capet, X., Debreu, L., & Benshila, R. (2016). On effective resolution in ocean models. *Ocean Modelling*, *98*, 36–50. https://doi.org/10.1016/j.ocemod.2015.12.004

Tedesco, P., Gula, J., Penven, P., & Ménesguen, C. (2022). Mesoscale eddy kinetic energy budgets and transfers between vertical modes in the Agulhas Current. *Journal of Physical Oceanography*, *52*(4), 677–704. https://doi.org/10.1175/jpo-d-21-0110.1

Venaille, A., Vallis, G., & Smith, K. (2011). Baroclinic turbulence in the ocean: Analysis with primitive equation and quasigeostrophic simulations. *Journal of Physical Oceanography*, *41*(9), 1605–1623. https://doi.org/10.1175/jpo-d-10-05021.1

Wunsch, C. (1997). The vertical partition of oceanic horizontal kinetic energy. *Journal of Physical Oceanography*, *27*(8), 1770–1794. https://doi.org/10.1175/1520-0485(1997)027<1770:tvpooh>2.0.co;2

Wunsch, C. (2007). The past and future ocean circulation from a contemporary perspective. *Geophysical Monograph-American Geophysical Union*, *173*, 53.

Yan, X., Kang, D., Curchitser, E., & Pang, C. (2019). Energetics of eddy–mean flow interactions along the western boundary currents in the North Pacific. *Journal of Physical Oceanography*, *49*(3), 789–810. https://doi.org/10.1175/jpo-d-18-0201.1

Yang, Y., & Liang, X. S. (2016). The instabilities and multiscale energetics underlying the mean–interannual–eddy interactions in the Kuroshio Extension region. *Journal of Physical Oceanography*, *46*(5), 1477–1494. https://doi.org/10.1175/jpo-d-15-0226.1

Yang, Z., Zhai, X., Marshall, D., & Wang, G. (2021). An idealized model study of eddy energetics in the western boundary "graveyard". *Journal of Physical Oceanography*, *51*(4), 1265–1282. https://doi.org/10.1175/jpo-d-19-0301.1

Yankovsky, E., Zanna, L., & Smith, K. (2022). Influences of mesoscale ocean eddies on flow vertical structure in a resolution-based model hierarchy. *Earth and Space Science Open Archive*, *60*. https://doi.org/10.1002/essoar.10511501.1

Zhai, X., Johnson, H., & Marshall, D. (2010). Significant sink of ocean-eddy energy near western boundaries. *Nature Geoscience*, *3*(9), 608–612. https://doi.org/10.1038/ngeo943